AGU PUBLICATIONS

JGR

Journal of Geophysical Research: Solid Earth

RESEARCH ARTICLE
10.1002/2017JB014509

The Effective Transmissivity of a Plane-Walled Fracture With Circular Cylindrical Obstacles

Lukasz Jasinski[1] and **Marcin Dabrowski**[1,2]

[1] Computational Geology Laboratory, Polish Geological Institute-National Research Institute, Wroclaw, Poland, [2] Physics of Geological Processes, University of Oslo, Oslo, Norway

Key Points:
- The Brinkman fracture flow model captures well the Stokes flow in a plane-walled fracture with circular cylindrical inclusions
- The analytical model of Kumar et al. (1991) provides a good approximation to the numerical results
- The model can be used for predicting the effective transmissivity of a propped fracture

Correspondence to:
L. Jasinski,
lukasz.jasinski@pgi.gov.pl

Citation:
Jasinski, L., & Dabrowski, M. (2018). The effective transmissivity of a plane-walled fracture with circular cylindrical obstacles. *Journal of Geophysical Research: Solid Earth*, *123*, 242–263. https://doi.org/10.1002/2017JB014509

Received 1 JUN 2017
Accepted 20 DEC 2017
Accepted article online 2 JAN 2018
Published online 22 JAN 2018

Abstract Stimulated and propped fractures provide the conductive pathways in low matrix permeability rocks. We study the impact of fracture aperture and proppant size and fraction on the effective transmissivity of a stimulated fracture filled with a partial monolayer of proppant grains. The proppant grains are treated as circular cylindrical obstacles, and the fracture walls are planar. The key geometric parameters are the obstacle fraction f and the ratio between the fracture aperture and the obstacle diameter α. We use three-dimensional Stokes flow numerical simulations to demonstrate that the fracture flow model given by the Reynolds equations may largely overestimate the flow rate. To circumvent the inability of the Reynolds model to fulfill the no-slip boundary condition at the rims of the obstacles, we use the Brinkman flow model adapted to the case of fracture flow. The relative difference between the effective transmissivities computed with the Stokes and Brinkman models for systems with multiple obstacles is below 10% for fractions up to 0.5. We use the Brinkman model to study the effective transmissivity of a plane-walled fracture with circular cylindrical obstacles. Systematic numerical simulations show that the normalized effective transmissivity is predominantly dependent on f and α, and the effects of obstacle ordering are minor. The presented numerical results can be used by petroleum engineers for estimating transmissivities of propped fractures under in situ conditions. The model can also be applied to microfluidic systems and for deriving first-order estimates of the effective transmissivity of rough-walled, natural fractures with load-bearing contact areas.

1. Introduction

Fracture flow is the prime mechanism of fluid transport in low matrix permeability formations, for example, shales and crystalline rocks. It may play an important role during natural processes such as hydrocarbon migration (Aydin, 2000), hydrothermal circulation (Andersen et al., 2015; Curewitz & Karson, 1997; Lupi et al., 2010), and metamorphism (Bickle & McKenzie, 1987; Jamtveit & Yardley, 1997). Fracture flow can also be a key factor in industrial applications. A detailed knowledge of the transport properties of a fracture network is required to ensure long-term gas storage in caverns in granitic rocks (Lindblom, 1989; Yoshida et al., 2013) and to assess the safety of radioactive waste repositories in cystalline rocks (Neretnieks, 1990; Pruess et al., 1990). Similarly, a detailed characterization of the flow properties of both single fractures (Méheust & Schmittbuhl, 2001; Mourzenko et al., 1996; Renard et al., 2006) and fracture networks (Berkowitz & Adler, 1998; Odling, 1997) is needed to build a model of a reservoir. Fracture transmissivity is an essential property that controls production efficiency in the oil and gas industry, especially in low-permeability reservoirs (King, 2010; Palisch et al., 2010; Warpinski et al., 2009).

Based on laboratory and in situ permeability measurements for crystalline and argillaceous rocks, Brace (1980) discussed the influence of burial depth on the overall permeability of rock fractures. Berkowitz (2002) reviewed state-of-the-art measurements and mathematical models of flow and transport phenomena in fractured rock. The permeability of natural fracture networks is often too low for industrial processes, and both geothermal energy extraction from low-permeability crystalline rocks and oil and gas recovery from tight and shale gas reservoirs can be enhanced by hydraulic fracturing. Injection of high-pressure fluids into rock formations produces new surfaces and promotes opening of the existing fractures, increasing the surface area contributing to hydrocarbon or geothermal energy production (King, 2010; Legarth et al., 2005). Proppant slurries are often pumped into the induced and stimulated fractures to maintain their apertures

once fluid pressure is released (Liang et al., 2016; Zimmermann & Reinicke, 2010), and technological fluids are mediated through propped fractures during the production phase in unconventional reservoirs and geothermal fields.

Fracture roughness has a major impact on flow efficiency in natural fractures (Brown, 1987; Lee et al., 2014; Mourzenko et al., 1995; Pyrak-Nolte et al., 1987; Zimmerman & Bodvarsson, 1996). However, for most technological fractures, the main resistance to flow is posed by proppant obstacles, and fracture surface roughness is likely to play a subordinate role. The transmissivity of a propped fracture has been studied experimentally (Cooke, 1973; Zhang et al., 2015) and numerically (Khanna et al., 2012). It was already demonstrated by Darin and Huitt (1960) that a partial monolayer of proppants provides transmissivity that otherwise would require several proppant layers, and monolayer proppant arrangements can be achieved by selecting lightweight proppants and low-viscosity fluids (Brannon et al., 2004; Ramurthy et al., 2013). Proppant grains can experience embedment into the rock matrix due to high confining pressures, which can significantly reduce fracture aperture and have a detrimental effect on the transmissivity of a propped fracture. Alramahi and Sundberg (2012) showed that the embedment process is particularly significant for clay-rich rocks, which are prone to creep, and the monolayer configuration of proppant grains.

The problem of flow in narrow apertures with obstacles has been gathering attention for over a hundred years. Hele-Shaw (1898) performed a series of experimental studies of the steady state viscous flow past cylindrical obstacles embedded between parallel planar plates. For narrow apertures, the observed flow was laminar and resembled the theoretical flow of an inviscid fluid around an infinite cylinder, except in the direct vicinity of the obstacles, where boundary layers formed. Neglecting inertia effects and assuming that the velocity component perpendicular to the walls is small compared to the in-plane components, Stokes (1851) derived, to leading order, a simplified flow equation, which stated that the wall-perpendicular component of velocity vanishes, the velocity is given by pressure gradient, and the pressure is constant across the aperture and harmonic in the wall plane. The same partial differential equation was independently proposed earlier in the context of thin viscous fluid films by Reynolds (1886). Stokes recognized that the assumptions, which allowed for deriving a simplified, reduced-order approach, led to the inability of satisfying the no-slip condition at the rims of the obstacle. In particular, the in-plane components of the second-order derivatives of the velocity vector are not necessarily negligible in the vicinity of the obstacle.

Thompson (1968) presented an expansion solution of the Stokes flow around an isolated circular obstacle confined between two parallel plates. The velocity field was given for small ratio between the plate separation and obstacle diameter. Lee and Fung (1969) derived a more general series solution, whose convergence was examined for the distance between the plates reaching 5 times the diameter of the obstacle. An approximate solution was obtained by retaining only two leading-order terms in the expansion, and it was shown to perform well for the distance between the plates not exceeding the diameter of the obstacle. The two-term approximation was further asymptotically expanded in the limit of small plate separation, and it was found to favorably compare to the Thompson's solution. Lee (1969) extended the approximate two-term solution to develop a periodic solution for regularly spaced circular obstacles between parallel plates. The solution was used to find the resistance of the flow as a function of geometric parameters. Balsa (1998) used a combination of matched asymptoptic expansions and a numerical method to obtain the correction term taking into account the no-slip boundary condition at inclusion rims into the classical Hele-Shaw expression.

Spielman and Goren (1968) and Pop and Cheng (1992) presented analytical studies of the incompressible steady state flow past a circular cylinder embedded in a porous medium using the Brinkman model (Brinkman, 1949), which allows for satisfying the no-slip boundary condtion at the rim of the cylinder. Although fracture flow is not considered in the original study, the derived analytical models can be used to obtain an approximation to the flow around a circular obstacle embedded in a narrow aperture by supplying it with the permeability of an empty fracture rather than the permeability of a homogeneous three-dimensional porous medium. A similar derivation was presented by Wang (2009) and was used to build an effective medium model of the pressure drop for multiple inclusions with a minimum separation large enough to neglect mutual interactions. An approximate, depth-integrated Brinkman-type fracture flow model was used by Fernandez et al. (2001) to derive a linear stability analysis of viscous fingering inside the Hele-Shaw cell. Zeng and Weinbaum (1994) provided a detailed analysis of the Brinkman correction for unidirectional flows in a Hele-Shaw cell.

The authors showed that although the correction should in general involve a nonlocal operator of the averaged velocity, using the local Laplace term scaled by the inverse of the background permeability of the cell is a good approximation at long wavelength.

Kumar et al. (1991) investigated fluid flow between two parallel plane walls with randomly distributed, monodisperse cylindrical obstacles, which were considered as an analog of contact areas in natural rock fractures. The authors developed an expression for the overall permeability by deriving and integrating the fracture-perpendicular distribution of the average velocity. The approach builds on the effective permeability due to in-plane averaging for an unbounded system consisting of infinitely long cylinders. Interestingly, a Brinkman-type equation arises again during the depth integration of the in-plane averaged velocity. The authors claimed that their estimate provides a very good fit to the experimental results. The same result, although in a different context, was also obtained by Tsay and Weinbaum (1991).

The Brinkman model of fracture flow has also been used in numerical simulations. Flekkøy et al. (1995) studied the hydrodynamic dispersion around a single cylindrical obstacle in a Hele-Shaw cell using both experiment and Lattice Boltzman numerical simulations. While reducing the dimensionality of the problem and deriving an approximate flow model, the authors treated the viscous drag effect due to the walls by assuming a perfectly parabolic shape of the velocity profile across the thickness of the cell, which led them to the Brinkman model. Using an analytical solution for the open channel flow, the accuracy of the approximate flow model was assessed at about 10%. The Brinkman model was also used for modeling two phase flows in a Hele-Shaw cell with cylindrical obstacles (Ferrari et al., 2015; Horgue et al., 2013). Nagel and Gallaire (2015) used a boundary element method (BEM) to solve the Brinkman model for a deformable droplet in a microfluidic flow in a narrow channel. Laleian et al. (2015) used 2-D and 3-D lattice Boltzmann method (LBM) simulations to study the accuracy of the depth-averaged flow model for variable aperture and cylindrical obstacles of different size, reporting an accuracy of 10% in terms of the effective permeability.

The Brinkman flow model can be viewed as combining the Stokes model, which governs the flow in pure fluid regions at the microscale, and the Darcy model, which describes the macroscopic flow in porous media. The Brinkman fracture flow model can be obtained from the two-dimensional Stokes model by adding a velocity-proportional linear term due to the wall resistance. Such approach allows for using the no-slip boundary condition at the rims of the obstacles. On the other hand, the classical Reynolds model, or the local cubic law (LCL), is widely used for flow description in fractures. It can be derived from the Stokes equations assuming a constant pressure across the fracture aperture and a smooth variation of fracture aperture. Various approaches to measuring the local fracture aperture and including fracture tortuosity have been proposed to improve the performance of the Reynolds model (Brown, 1987; Brush & Thomson, 2003; Ge, 1997; Lee et al., 2014; Mallikamas & Rajaram, 2010; Mourzenko et al., 1995; Oron & Berkowitz, 1998; Renshaw, 1995; Wang, Cardenas, et al., 2015; Yeo, 2001; Zimmerman & Bodvarsson, 1996). However, due to a reduced-order approach, the Reynolds model cannot satisfy the no-slip condition at the contacts. Although the local cubic law model has been often used to study the influence of contacts on the flow in rough-walled fractures (see for a review, e.g., Dippenaar & Rooy, 2016), already at low obstacle fractions, the contact regions may influence flow paths more significantly than predicted in the LCL models (Berkowitz, 2002; Durham & Bonner, 1994; Oron & Berkowitz, 1998)

In the present work, we focus on the idealized fracture bounded by parallel planar walls and filled with circular obstacles. The studied geometry can directly represent hydraulic fractures propped with large proppant grains (Alramahi & Sundberg, 2012; Brannon et al., 2004), or it can be a good approximation to fractures formed by reactive processes (Budek et al., 2017; Detwiler et al., 2003; Szymczak & Ladd, 2009). We use the 2.5-D Brinkman flow model, which ensures the satisfaction of the no-slip boundary condition at the rims of the obstacles, to perform numerical simulations of the flow transmissivity of an idealized fracture. The numerical model is validated against an analytical solution in the case of an isolated circular obstacle. We carry out direct numerical simulations using a three-dimensional finite element incompressible Stokes solver for both fractures with mutliple obstacles to validate the accuracy of the approximate 2.5-D solutions based on either the Stokes-Brinkman or the Reynolds model. Then, systematic simulations of the transmissivity tensor are conducted using the Brinkman model for a wide range of obstacle fractions and various fracture aperture to grain diameter ratios. The computed transmissivities are compared with the predictions of the effective medium approximations.

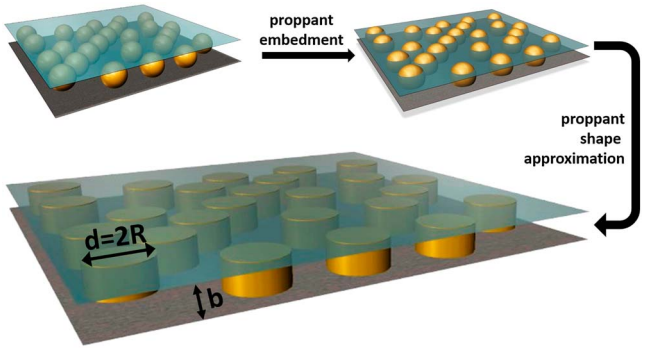

Figure 1. A geometric model of a plane-walled fracture filled with randomly located cylindrical circular obstacles. The cylindrical obstacles approximate embedded proppant grains of a spherical shape. *b* denotes the fracture aperture, and *R* and *d* are the cylindrical obstacle radius and diameter, respectively.

2. Model

2.1. A Geometric Model of a Fracture With Obstacles

Figure 1 shows our geometric model of a plane-walled fracture supported by randomly distributed circular cylinders, which may correspond to a partial monolayer of proppant grains. We postulate that spherical proppant grains appear as cylindrical circular obstacles due to their embedment into the wall rock under high confining pressures. A parameter α is introduced to characterize the level of proppant embedment

$$\alpha = \frac{b}{d} \tag{1}$$

where b is the fracture aperture and d is the obstacle diameter. We use R to denote the obstacle radius, and f is the surface fraction occupied by the obstacles in 2-D. For cylindrical obstacles, the areal fraction is equivalent to the volumetric fraction.

The obstacles are assumed to be monodisperse throughout the model. Although for embedding proppant grains, we expect α to be less than 1, higher values may be relevant to other applications. Hence, we use α up to 5 in our simulations. To obtain two-dimensional distributions of nonoverlapping circular obstacles, we use the following:

1. *RSA*. Random Sequential Adsorption algorithm, in which disks are sequentially placed at random locations and only nonoverlapping disks are added to the model. Using RSA, a maximal packing limit $f_c = 0.547 \pm 0.002$ can be reached in an unbounded two-dimensional domain. The details of the algorithm are present in Feder (1980). We enforce a minimal separation of $0.05R$ between the disks, which allows us to obtain packing fractions of up to about $f = 0.5$ with RSA.
2. *LSA*. Modified Lubachevsky-Stilinger algorithm (e.g., Skoge et al., 2006), in which initially small disks, seeded with a Poisson distribution in space, are grown to a desired fraction, while their positions are redistributed in energy-dissipating collisions to ensure no overlaps. Again, a minimal separation of $0.05R$ between the disks is enforced, and packing fractions of up to $f = 0.8$ can be obtained.
3. *HCP*. Hexagonal packing arrangement, in which the maximum packing fraction for such configuration is $f = \pi/(2\sqrt{3}) \approx 0.9069$ (e.g., Berryman, 1983). In our numerical simulations, we have generated packings up to fraction of $f = 0.905$.

In 3-D and the corresponding 2.5-D simulations, we use nonperiodic distributions of the obstacles; that is, the cylinders are fully contained within a square computational domain. Otherwise, we use periodic distributions with a square unit domain, whose boundaries are in general intercepted by the obstacles. We presented examples of periodic obstacle distributions generated with RSA, LSA, and HCP in Figure 2.

2.2. Fracture Flow Models

We assume that the flow is in the laminar regime, that is, the Reynolds number *Re* is small. We also consider a low Knudsen number regime, in which the no-slip boundary condition applies at the solid-fluid interfaces

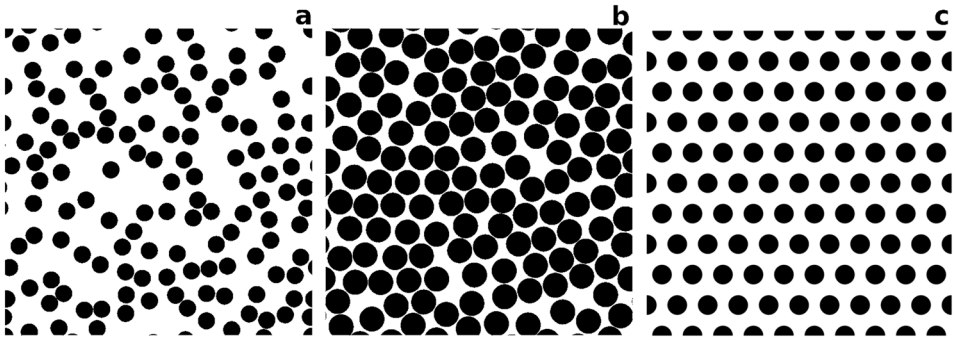

Figure 2. Selected examples of periodic obstacle distributions generated using (a) RSA, (b) LSA, and (c) HCP. The obstacle fraction is 0.3 in Figure 2a, 0.65 in Figure 2b, and 0.3 in Figure 2c.

(e.g., Landau and Lifshitz, 1959). Lauga et al. (2007) and Wang, Schmitt, and Wang (2015) described the limitations of using the no-slip boundary conditions.

2.2.1. The 3-D Stokes Model

Low Reynolds number flows are governed by the three-dimensional Stokes equations

$$-\nabla p + \mu \nabla^2 \mathbf{u} + \mathbf{f} = 0 \tag{2}$$

$$\nabla \cdot \mathbf{u} = 0 \tag{3}$$

where p is fluid pressure, $\mathbf{u}$ is the velocity vector, $\mathbf{f}$ is the body force, and μ denotes the fluid shear viscosity. In equation (2), we assume that the fracture is filled with a single-phase, incompressible Newtonian fluid, which is characterized by a constant viscosity. We use the 3-D Stokes model to perform direct numerical simulations, in which fluid flow is computed using the exact three-dimensional fracture geometry. However, solving the incompressible Stokes equations for complex fracture geometries poses certain numerical challenges. Therefore, we seek an appropriate 2.5-D upscaled flow model, which could be used during systematic simulations for representative systems with a large number of obstacles ($N > 1{,}000$).

For technical reasons, we use nonperiodic obstacle distributions in our 3-D Stokes simulations. Thus, no obstacles intercept the boundaries of a regular computational box. We drive the flow by imposing a background pressure gradient, which is achieved by accordingly prescribing the normal component of the traction vectors at the upstream and downstream model boundaries. The tangential components of the velocity vectors are set to 0 at these walls. The no-slip boundary conditions are used at the remaining boundaries, that is, the other pair of the side walls, the top and bottom fracture walls, and at the rims of the obstacles.

2.2.2. The 2.5-D Brinkman Model

The Stokes equation (equation (2)) can be integrated across the fracture depth assuming locally parabolic velocity profiles, as it was, for example, proposed in Flekkøy et al. (1995). As a result, we obtain a Brinkman type of equations

$$-b\nabla p + \mu \nabla^2 \mathbf{J} - \frac{\mu}{K}\mathbf{J} + b\mathbf{f} = 0 \tag{4}$$

$$\nabla \cdot \mathbf{J} = 0 \tag{5}$$

where $\mathbf{J}$ is the local flow rate (i.e., the depth-integrated in-plane components of the velocity vector), and K is the permeability of an empty plane-walled channel of an aperture b, $K = 1/12b^2$. The additional Brinkman term $\frac{\mu}{K}\mathbf{J}$ in equation (4) corresponds to the viscous drag due to the presence of the fracture walls.

We use the Brinkman model in our systematic simulations of the effective fracture transmissivity for periodic distributions of the obstacles. In the simulations, periodic boundary conditions are applied in both x and y directions, and fracture flow is driven by a prescribed body force $\mathbf{f}$. In the Brinkman model, the no-slip boundary conditions can be prescribed to the rims of the obstacles. The no-slip boundary conditions are also implicitly used at the fracture walls.

2.2.3. The 2.5-D Reynolds Model

Fracture flow is typically described using the Reynolds model (e.g., Adler & Thovert, 1999)

$$\mathbf{J} = \frac{b^3}{12\mu}\left(-\nabla p + \mathbf{f}\right) \tag{6}$$

$$\nabla \cdot \mathbf{J} = 0 \tag{7}$$

The Reynolds model is governed by a scalar-valued partial differential equation, which is an appreciable simplification over the vector-valued Stokes model. However, it only allows for applying the free-slip rather than the no-slip boundary conditions, which is expected to result in a significantly overestimated flow rate in fractures with a large fraction of obstacles.

2.3. Finite Element Method Flow Solvers

The Brinkman model (equations (4) and (5)) is solved numerically using a modified MILAMIN code. MILAMIN (Dabrowski et al., 2008) is a finite element method (FEM)-based incompressible Stokes solver based on the mixed formulation, which is capable of solving two-dimensional problems on unstructured computational meshes. We run Triangle (Shewchuk, 1996) to discretize the void space between the obstacles with body-fitting triangular meshes. MUTILS package (Krotkiewski & Dabrowski, 2013) is used to call Triangle directly in MATLAB, without using any file I/O. The second-order, Ladyzenskaja-Babuska-Brezzi (LBB)-stable

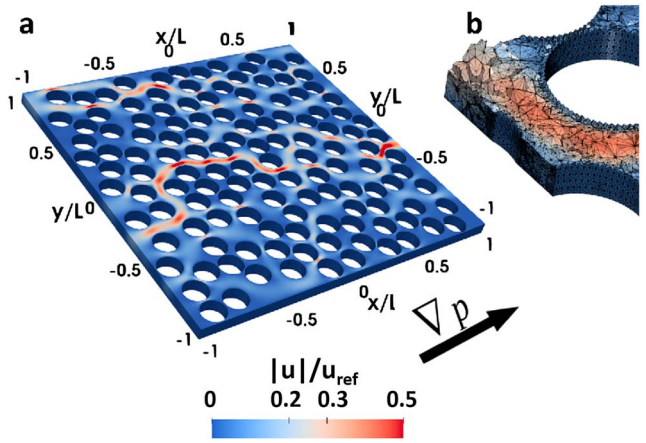

Figure 3. (a) An example of the three-dimensional Stokes model. The peak velocity magnitude u normalized by the reference flow rate u_{ref} in an empty fracture is color-coded. (b) A zoomed portion of the model, illustrating the computational mesh.

seven-node Crouzeix-Raviart triangular element with a linear discontinuous pressure is used. The FEM discretization of the Brinkman model gives in an indefinite, symmetric system of linear equations

$$\begin{pmatrix} A & B^T \\ B & 0 \end{pmatrix} \begin{pmatrix} v \\ p \end{pmatrix} = \begin{pmatrix} f \\ g \end{pmatrix} \tag{8}$$

where v and p denote the discrete velocity (depth-integrated) and pressure (scaled with the fracture aperture), B is the discrete divergence operator, and f and g are the right-hand side terms taking into account the body force and the Dirichlet and Neumann boundary conditions. The A operator is given by the sum of the velocity stiffness matrix scaled by the fluid viscosity and the velocity mass matrix scaled by μ/K, which corresponds to the Brinkman term in equation (4). A block Gaussian elimination of equation (8) results in a symmetric, positive-definite pressure Schur complement

$$BA^{-1}B^T p = BA^{-1}f - g \tag{9}$$

We avoid explicitly computing the pressure Schur complement, and the conjugate gradient iterations preconditioned with the pressure mass matrix M are used to solve equation (9). To reduce the number of iterations, we improve the conditioning of the pressure Schur complement by adding a penalty term $\kappa B^T M^{-1} B$ to the A matrix, where κ denotes the penalty factor. For a discontinuous pressure space, M can be inverted on the element level, and the inner matrix $A + \kappa B^T M^{-1} B$ can be formed explicitly and factorized by the Cholesky decomposition as it remains sparse, symmetric, and positive definite. Despite its nonlinear scaling, highly efficient modern implementations of the sparse Cholesky factorization can be used in practice for systems with up to several tens of millions of degrees of freedom, if preceded with an appropriate fill-in reducing reordering. The time spent on the factorization, which dominates the computation time, is on the order of 1 min for systems with 1 million computational nodes. During pressure iterations, the action of the inverse of the inner matrix is found by applying the forward and backward substitutions to the Cholesky factor, which is computed once and stored. Increasing the penalty factor generally reduces the number of iterations. However, a too high penalty factor may result in an ill conditioning of the inner system. We have also noticed that the simple mass matrix preconditioning deteriorates for models with a small permeability (fracture aperture). The velocity field can be easily recovered, once the pressure is found.

We use TetGen (Si, 2015) to generate unstructured tetrahedral meshes (Figure 3b), which are used in our 3-D Stokes simulations. MUTILS package (Krotkiewski & Dabrowski, 2013) is again used to call TetGen directly in MATLAB. Due to a higher nodal connectivity, the Cholesky factorization is impractical for 3-D problems. Instead, we use the minimal residual (*minres*) iterations directly on the indefinite system (equation (9)), setting κ to 0 or a small value. The *minres* iterations are preconditioned by either a simple Jacobi or a two-level Bramble-Pasciak-Xu (BPX) type of the preconditioner for the A block and the pressure mass matrix for the remaining part. The sparse matrix vector multiplications are performed with a NUMA-aware routine from the MUTILS package, which allows us to use a tailored blocked storage for the symmetric sparse matrix and reach an almost optimal memory bandwidth during the computations.

In Figure 3 we present an example solution of flow in a plane-walled fracture with 128 circular cylindrical obstacles using three-dimensional Stokes model. The obstacle positions are generated using RSA algorithm in which the fraction is $f = 0.5$ and the fracture aperture to obstacle diameter ratio is equal to 1. The flow is driven by a nonzero pressure gradient applied to the opposite walls in the x direction ($\nabla p = (p_2 - p_1)/L$, where p_2 and p_1 are constant pressures applied at the walls yz at $x = 0$ and $x = L$, respectively, and $p_2 > p_1$). The no-slip boundary condition is used at the rims of the obstacles, at the lateral walls in the y direction, and at the fracture wall. Only a bottom half of the fracture aperture is modeled due to the presence of mirror symmetry about the midplane, where we apply the free-slip boundary condition.

2.4. Effective Fracture Permeability and Transmissivity

The specific discharge q_x in x direction through an arbitary yz plane $-L < x < L$is defined by the following integral

$$q_x(x) = \frac{1}{2Lb} \int_{-b/2}^{b/2} \int_{-L}^{L} u_x(x, y, z) \mathrm{d}y\mathrm{d}z \tag{10}$$

where u_x denotes the x component of the velocity vector and L is a half-length of the computational box. For an incompressible flow, the discharge q_x integrated on yz plane is independent of x, and any fluctuations are due to numerical resolution. The integral (equation (10)) can be evaluated by performing Gaussian quadratures on a set of triangles due to intercepting the tetrahedral mesh with a given yz plane (intercepting a tetrahedron with a plane results in either a triangle or a quadrangle, which can be subdivided into two triangles). In the case of 2.5-D models, the depth integration can be performed analytically by invoking the parabolic profile, and the numerical integration is used for the individual segments of the line that cuts the triangles from the mesh. The K_{xx} component of the effective fracture permeability tensor is given by

$$K_{xx} = \frac{2L\mu}{\Delta p} q_x \tag{11}$$

where Δp denotes the pressure difference applied in the x direction. The off-diagonal K_{xy} component is given by

$$K_{xy} = \frac{2L\mu}{\Delta p} q_y \tag{12}$$

where the pressure difference is still applied in the x direction and the specific discharge q_y in y direction can be defined in an analogous way as q_x. The complete effective fracture permeability tensor

$$\mathbf{K} = \begin{bmatrix} K_{xx} & K_{xy} \\ K_{yx} & K_{yy} \end{bmatrix} \tag{13}$$

can be obtained by computing the specific discharges for two independent flows imposed with pressure gradients acting in the perpendicular directions, namely x and y. Then, the eigenvalues K_1 and K_2 of the permeability tensor (equation (13)) can be obtained and ordered as $K_1 > K_2$. The anisotropy of the effective fracture permeability can be characterize by the anisotropy factor

$$\delta = \frac{K_1}{K_2} \tag{14}$$

The mean permeability can be defined as the geometric mean of the principal permeabilities

$$K = \sqrt{K_1 K_2} \tag{15}$$

The effective fracture transmissivity σ can be obtained by scaling the effective fracture permeability K with the fracture aperture b.

3. Analytical Solution for Brinkman Flow Around an Isolated Cylinder

We use the analytical model of Spielman and Goren (1968) for Brinkman flow around an isolated impermeable cylinder to validate our Stokes-Brinkman 2.5-D (section 4.1.1) and to obtain the effective medium theory estimates (section 5). The solution was rederived and applied in several other works (e.g., Chernyakov, 2001; Pop & Cheng, 1992; Wang, 2009). Wang (2009) presented the Brinkman equation (a distinction between the effective viscosity of porous media and the fluid viscosity is made in the original paper of Wang, 2009) in a dimensionless form by introducing a characteristic length scale R (inclusion radius), velocity U_0, and pressure $\mu U_0/R$

$$\nabla p' = \nabla^2 \mathbf{u}' - s^2 \mathbf{u}' \tag{16}$$

The parameter s is a dimensionless parameter representing the ratio between the obstacle radius and the length scale derived from the permeability of porous medium

$$s^2 = \frac{R^2}{K} \tag{17}$$

In our fracture flow model, the permeability is given by the permeability of an empty fracture

$$s^2 = 12\left(\frac{R}{b}\right)^2 = 3\alpha^{-2} \tag{18}$$

A uniform flow is considered in the far field, and no-slip boundary conditions are invoked at the rim of the cylinder. The solution to the problem can be found using the stream function approach in cylindrical coordinates

$$\psi(r,\theta) = f(r)\sin\theta \tag{19}$$

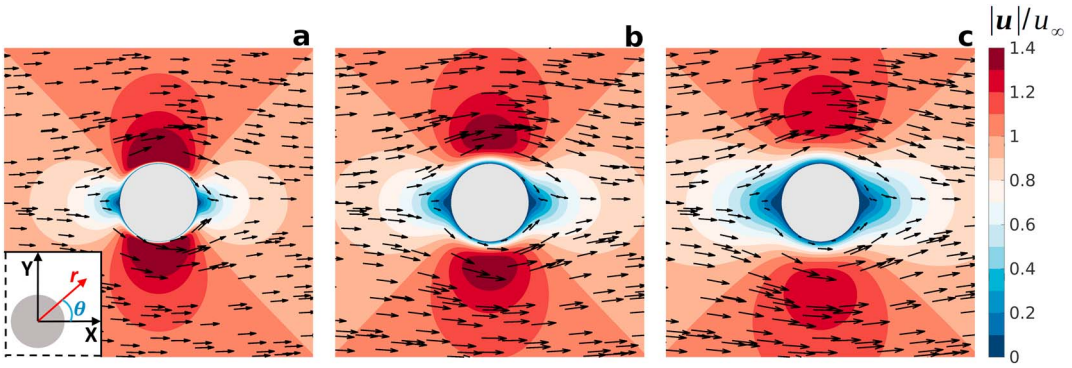

Figure 4. Two-dimensional Brinkman flow around an isolated impermeable circular inclusion subject to a uniform flow in the far field. The host permeability is given by the permeability of an empty fracture of an aperture equal to 2α times the inclusion radius. The depth-averaged velocity is normalized by the far-field flow rate, and its magnitude is color coded. The results are given for three different α values: (a) 0.1, (b) 0.5, and (c) 1.0. In the inset of Figure 4a the definition of r and θ in cylindrical coordinates is shown (equation (19)).

where the radial dependence is given by

$$f(r) = r - \left(1 + 2\frac{K_1(s)}{sK_0(s)}\right) \cdot \frac{1}{r} + \frac{2K_1(sr)}{sK_0(s)} \tag{20}$$

and K_0 and K_1 are the modified Bessel function of second kind. The velocity field can be calculated using the relation

$$\mathbf{u}' = \left(\frac{1}{r^2 \sin\theta}\frac{\mathrm{d}\psi(r,\theta)}{\mathrm{d}\theta}, -\frac{1}{\sin\theta}\frac{\mathrm{d}\psi(r,\theta)}{\mathrm{d}r}\right) \tag{21}$$

Finally, the net force acting on the cylinder is per unit width

$$D = 2\pi\mu U_0 \left(s^2 + \frac{2sK_1(s)}{K_0(s)}\right) \tag{22}$$

In Figure 4, we present the velocity field around an isolated circular inclusion using the analytical solution. The velocity is uniform in the far field, and the no-slip boundary condition is imposed at the rim of the inclusion. The results are presented for three selected α values: 0.1 (Figure 4a), 0.5 (Figure 4b), and 1.0 (Figure 4c). Increasing α (fracture aperture with respect to the inclusion diameter) results in a more distant perturbation of the velocity field but of a smaller amplitude. The regions of the highest velocity are visibly separated from the inclusions in the case of $\alpha = 0.5$ and $\alpha = 1.0$, while they are almost next to the inclusion for $\alpha = 0.1$, resulting in a steep velocity gradient. Although the magnitude of the velocity exhibits rather large differences between the models, the directions of the velocity vector remain quite similar.

4. Benchmarks

4.1. Flow Model Comparison

We compare the numerical solutions of the Stokes, Brinkman, and Reynolds flow models (section 2.2) for the simple case of an isolated cylinder and for RSA configurations with mutliple circular obstacles ($N = 128$). In this set of experiments, we use a square computational domain, which fully embeds all the obstacles, and we impose nonperiodic boundary conditions; that is, fluid flow is induced by a pressure difference applied between the two opposite sides of the sample in x direction, and the no-slip boundary conditions are used at the other pair of the side boundaries. To perform a direct comparison between the 3-D Stokes and 2.5-D Brinkman and Reynolds models, we evaluate the peak velocity field in the xy midplane of the three-dimensional Stokes model and obtain the corresponding quantity by scaling the local flow rate $\mathbf{J}$ in the 2.5-D models with $\frac{2}{3}b$.

4.1.1. A Plane-Walled Fracture With a Single Circular Obstacle

Figure 5 shows two perpendicular velocity magnitude profiles for flow around an isolated cylinder using $\alpha = 0.5$ (a, b) and $\alpha = 1.0$ (c, d). The profiles are taken along the lines $x = R/2$ (Figures 5a and 5c) and $y = R/2$ (Figures 5b and 5d). The velocity fields have been obtained for the Stokes, Brinkman, and Reynolds fracture

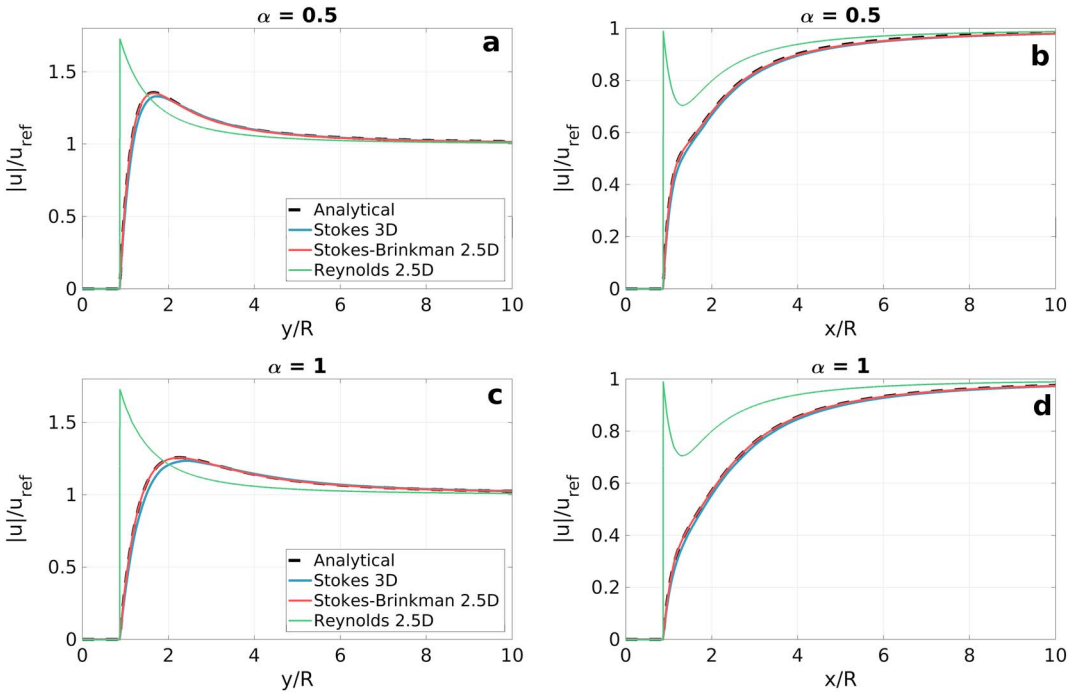

Figure 5. A comparison of velocity profiles along lines (a, c) $x = R/2$ and (b, d) $y = R/2$ for $\alpha = 0.5$ (Figures 5a and 5b) and $\alpha = 1.0$ (Figures 5c and 5d) obtained using a numerical solution of the Stokes model, analytical and numerical solutions of the Brinkman model, and an analytical solution of the Reynolds model. Only half of the profile is shown due to symmetry.

flow models. We show both the analytical and numerical solutions of the Brinkman model. The solutions practically coincide, and some minor discrepancies (not visible in the plots) can be related to a limited size of the computational domain rather than the discretization effect (a high numerical resolution was used). The Stokes and Brinkman models produce largely similar results; however, differences up to several percent are present in the high-velocity regions. We note that although the z component of the velocity vanishes by mirror symmetry in the midplane, it is nonzero away from it in the vicinity of the inclusion in the Stokes model. The result obtained with the Reynolds are notably different from all the other results, and, in particular, the velocity close to the obstacle tends to be high, which is a clear manifestation of the free-slip boundary condition.

4.1.2. A Plane-Walled Fracture With Multiple Circular Obstacles

In Figure 6, we show the velocity magnitude fields obtained numerically using the Stokes (a), Brinkman (b), and Reynolds (c) flow models for a plane-walled fracture with an obstacle fraction of $f = 0.3$ and an aperture-to-diameter ratio of $\alpha = 0.5$. One hundred twenty-eight obstacles are seeded using the RSA algorithm. The flow is driven by a pressure gradient applied to the left and right boundary walls, and the no-slip boundary condition is used at the rims of the obstacles and at the top and bottom lateral walls in the Stokes and Brinkman models. The flow fields obtained with the Stokes and Brinkman models are almost indistinguishable, and the flow pattern of disrupted channels of increased flow velocity can be observed. The Reynolds model produces a largely different flow field, which is characterized by the occurrences of high-velocity zones in the apertures parallel to the general flow direction between some of the neighboring obstacles. The velocity is clearly nonvanishing both at the rims of the obstales and at the top and bottom walls. The effective permeability in the direction of the imposed flow was calculated for the three models, resulting in $K_{3D}/R^2 = 2.05 \cdot 10^{-3}$, $K_{SB}/R^2 = 2.17 \cdot 10^{-3}$, and $K_R/R^2 = 4.24 \cdot 10^{-3}$ for the Stokes, Brinkman, and Reynolds models, respectively. The relative difference between the effective fracture permeabilities for the Stokes and Brinkman is about 5%. The effective permeability computed with the the Reynolds model overestimates twice the reference permeability obtained with the Stokes model. To gain insights into the character of the local differences, we plot the velocity magnitude profiles along the y direction at $x = 0$ (middle of the sample). The velocity profiles for the Stokes and Brinkman models are similar, and only minor differences, below 10% at maximum, can be observed. Although retaining an overall similarity, the velocity profile obtained with the Reynolds model exhibits some important differences. First, the velocities tend to be higher than in the other

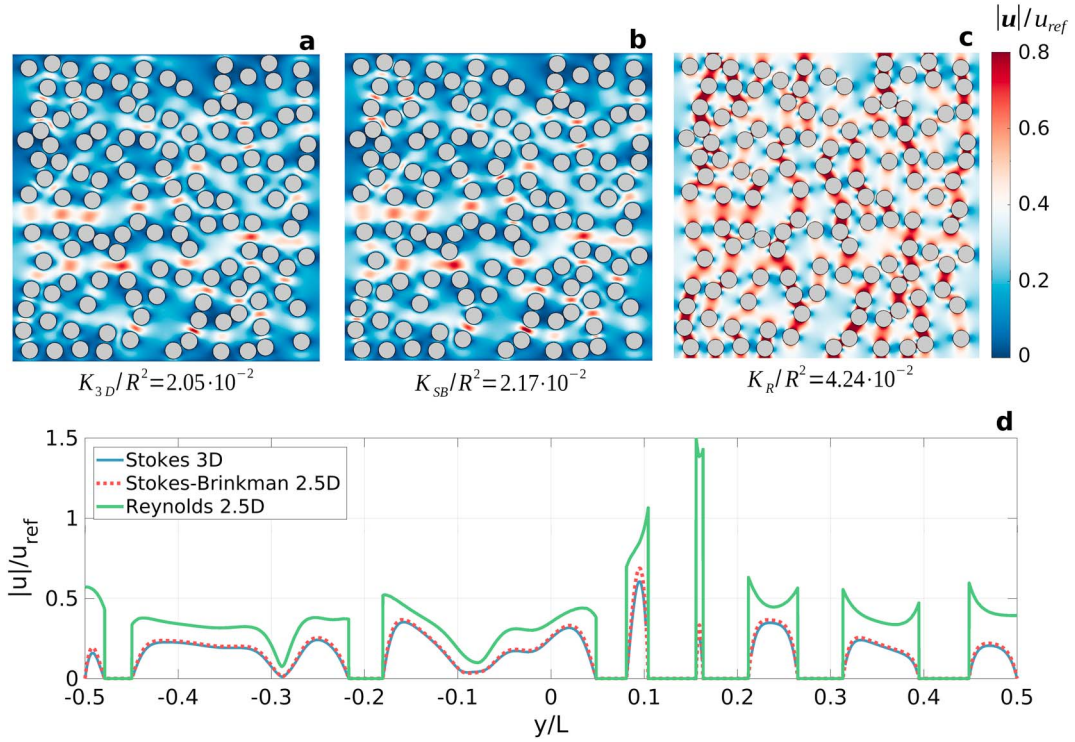

Figure 6. Flow field comparison between the (a) Stokes, (b) Brinkman, and (c) Reynolds models for a plane-walled fracture with an obstacle fraction of $f = 0.3$ and an aperture-to-diameter ratio of $\alpha = 0.5$. The 128 circular obstacles are generated with RSA. The velocity magnitude normalized by the reference flow rate for an empty fracture is color coded, and the normalized effective fracture conductivities are given. (d) Velocity magnitude profiles along y direction at $x/L = 0$ are displayed for the three models.

two models. Second, the velocity tends to decrease toward the center of the apertures giving the local maxima at the rims of the obstacles. A sixfold velocity increase can be observed in one of the apertures, resulting in a peak profile velocity. In Figure 7 we present a systematic comparison of the effective transmissivity computed with the upscaled models and the three-dimensional Stokes model for varying obstacle fraction between 0.1 and 0.5. In the test, we use 128 inclusions generated with RSA and a single realization for a given fraction. For the studied fraction range, the results show a steady increase of the mismatch between the upscaled models and the reference transmissivity obtained with the three-dimensional Stokes model. The mismatch reaches up to 10% in the case of the Brinkman model, and the effective transmissivity computed with the Reynolds model can be almost 25 times larger for $f = 0.5$ and $\alpha = 1.0$. At moderate fractions of about 0.3 the Reynolds model can overestimate the effective transmissivity by a factor of 4 ($\alpha = 1.0$). In our view, the discrepancy between the transmissivities computed with the Brinkman and Stokes model is on a sufficiently low level to consider the upscaled Brinkman model a satisfactory tool for performing systematic simulations for large systems. On the other hand, the Reynolds model produces largely overestimated results and should be avoided even for low obstacle fractions.

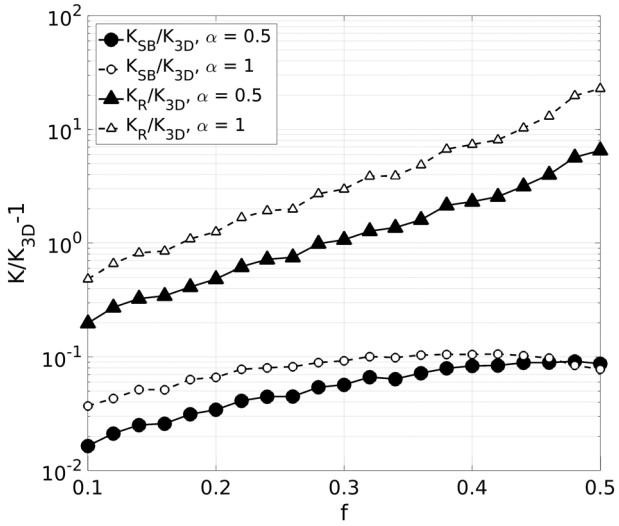

Figure 7. The relative difference between the effective fracture permeabilities computed for the upscaled Brinkman and Reynolds models and the three-dimensional Stokes model as a function of obstacle fraction. The results are shown for $\alpha = 0.5$ and 1.0 and obtained with a single realization for a given fraction using 128 obstacles generated with RSA.

4.2. System Size Effects

To quantify the system size effect, that is, the undesirable influence of a limited computational domain size L (with respect to the obstacle radius R) on the computed effective flow properties, we have performed systematic simulations varying the number of obstacles, that is, 64, 128, 256, 512, 1024, 2048 and finally 10000, while keeping the obstacle fraction fixed. We use obstacle fractions of 0.1, 0.3, and 0.5 for both RSA and LSA models

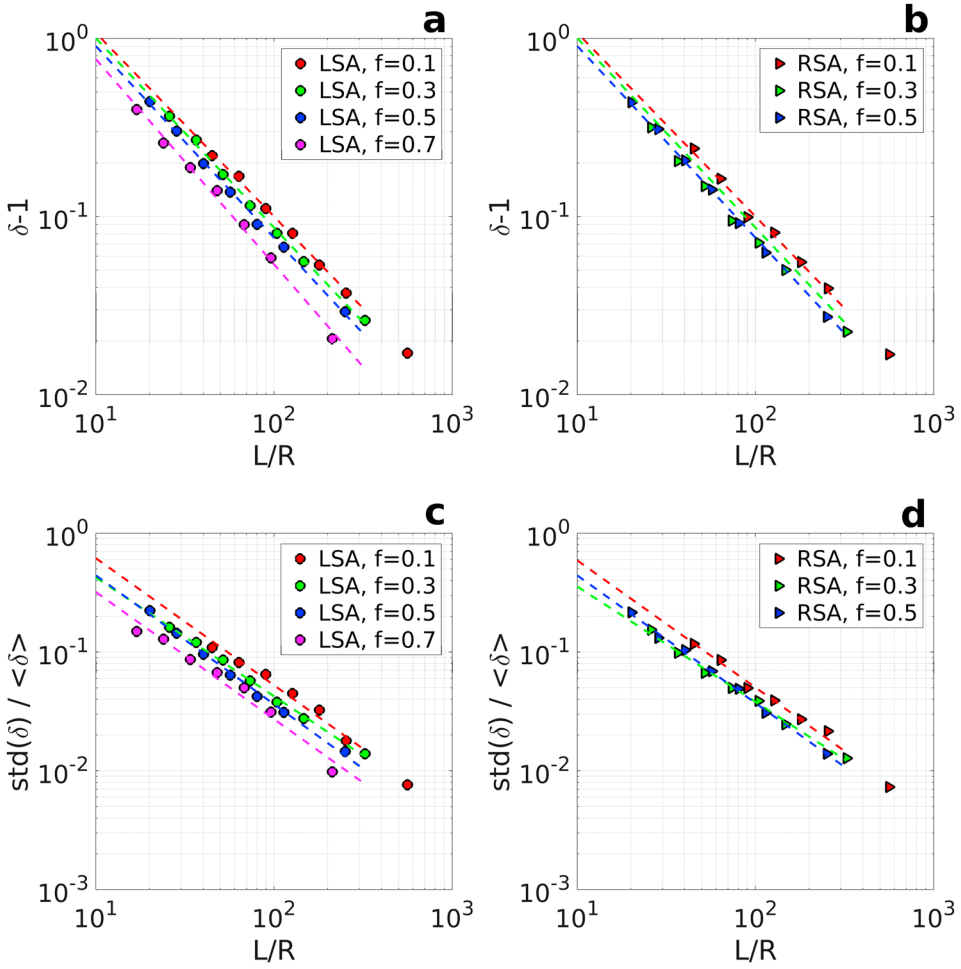

Figure 8. The (a, b) average and (c, d) standard deviation of the anisotropy factor computed for multiple realizations as a function of the normalized system size L/R. Dashed lines show power law fits.

and additonally 0.7 in the case of LSA. For each number of obstacles, 128 different realizations are generated to obtain the average values and standard deviations of the effective properties, with the exception of the largest system size ($N = 10{,}000$), for which only 16 different realizations are investigated.

4.2.1. Anisotropy

In Figures 8a and 8b, we present the average of a reduced anisotropy factor $\delta-1$ (see definition in equation (14) computed for multiple realizations as a function of system size L/R. The anisotropy factor reaches up to 1.5 for small system sizes, and it systematically decreases with increasing the system size. For a system size of about $L/R = 100$, the anisotropy factor is below 1.1. For any given system size, increasing obstacle fraction tends to give a lower degree of anisotropy. The lowest measured averages of the anisotropy factor yield about 1.02. We observe no substantial differences between the results for LSA and RSA. By fitting the system size dependence of the averaged anisotropy factor with a power law, we obtain $\delta - 1 \propto (L/R)^{-1}$. The power law fit is in agreement with the scaling proposed by Koza et al. (2009) for randomly generated 2-D porous media and generalized to the 3-D case by Matyka et al. (2013)

$$\delta - 1 \propto (L/R)^{-\frac{D}{2}} \tag{23}$$

where D is the system dimension.The standard deviation of the anisotropy factor (Figures 8c and 8d) exhibits the same scaling law. For a system size of $L/R = 100$, the normalized standard deviation of δ is already below 0.05.

4.2.2. Effective Permeability

Figures 9a and 9b show the effective mean permeabilities ($< K > = \sqrt{K_1 K_2}$ normalized by the mean value of permeability for the biggest system size, i.e., $N = 10{,}000$) and their standard deviations as a function of L/R

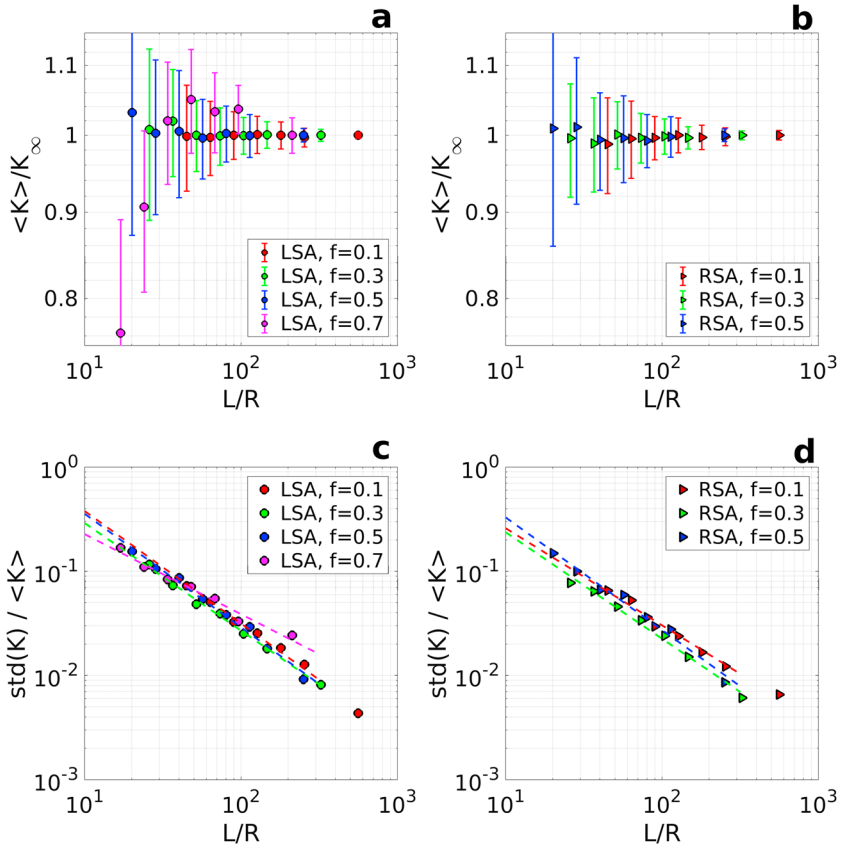

Figure 9. The (a, b) average and (c, d) standard deviation of the mean permeability computed for multiple realizations as a function of the normalized system size L/R. The standard deviation is also illustrated with the error bars (Figures 9a and 9b). Dashed lines show power law fits.

for various packing fractions f and two generation algorithms, that is, LSA and RSA. Figures 9c and 9d show the scaling of the standard deviation normalized by the average permeability as a function of the system size. For obstacle fractions below $f = 0.5$, the effective permeability exhibits clear convergence and the standard deviation decreases with increasing the system size, with the scaling approximately given by $(L/R)^{-1}$, similar to the one exhibited by the effective anisotropy. The standard deviation is less than 1% for $N = 10{,}000$, and it is less than 5% for 2,048 obstacles, which we consider as an acceptable level for further considerations. The standard deviation obtained for $N = 10{,}000$ and $f = 0.7$ gives a slightly outlying result, which may indicate that 16 is a too small number of samples for such high fraction.

5. Effective Transmissivity of a Fracture With Obstacles—Numerical Results and Effective Medium Theory

Figure 10 shows the effective transmissivity (the effective permeability K multiplied by the aperture b; see section 2.4) of a plane-walled fracture with circular cylindrical obstacles as a function of f for selected values of α. The results are given for 2,500 obstacles, whose positions are generated by either LSA, HCP, or RSA. We report the mean component of the effective transmissivity, according to equation (15). Both the obstacle distribution and the boundary conditions are periodic, and we use the Brinkman model to compute the flow field.

The effective transmissivity decreases with increasing f and decreasing α, which is an expected behavior due to a systematic reduction of the pore space available for the fluid flow. For $R \to 0$, the effective transmissivity $\frac{\sigma}{R^3} = \frac{2}{3}\alpha^3$ reproduces the solution for an empty fracture, that is, $\sigma = \frac{1}{12}b^3$. The effective transmissivities computed for RSA and LSA configurations, which can be compared up to a fraction of $f = 0.5$, show almost no difference. The LSA transmissivity curves exhibit evident plateaus while approaching $f = 0.7$, which is especially visible for high α ratios. On the other hand, the HCP curves show a monotonic behavior, with no plateau

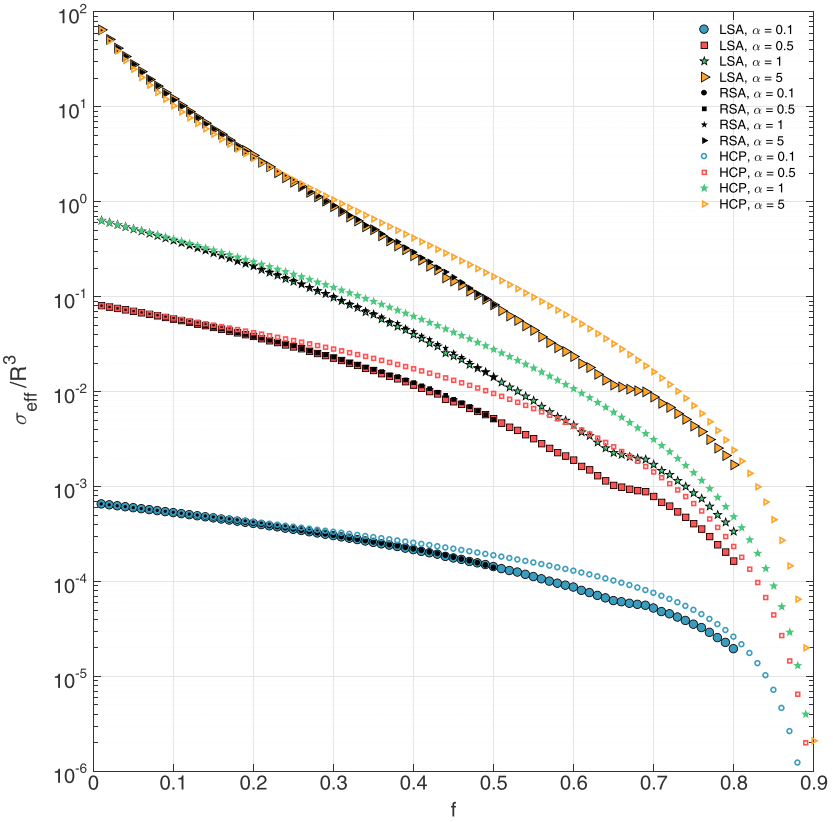

Figure 10. Normalized mean transmissivity $< \sigma > /R^3$ of plane-walled fractures with 2,500 circular cylindrical obstacles as a function of obstacle fraction f and fracture aperture to obstacle diameter ratio α. The obstacle distributions are produced using RSA, LSA, and HCP generation algorithms, and the results are obtained using numerical solutions of the Brinkman model.

regions, and the effective transmissivities obtained for the HCP configurations are systematically higher than the ones obtained for LSA. For moderate α values (0.5–1.0) and obstacle fractions of about $f = 0.65$, the results obtained for HCP can be 3 times higher than the LSA results. The HCP configuration guarantees that all the apertures between the obstacles systematically increase with decreasing packing fraction, which explains the strictly monotonic character of the HCP curves. In addition, the distances between the obstacles are more evenly distributed in the case of HCP, and in particular the minimal distance is larger than in the case of LSA configuration, which offers an explanation to systematically higher results for HCP. We hypothesize that the plateau observed in LSA curves relates to the onset of ordering, which is clearly present in LSA distributions for high fractions.

For a high aperture-to-diameter ratio of $\alpha = 5$, the effective transmissivity exhibits the largest dependence on the obstacle fraction, which for the studied range of fractions spans almost 5 orders of magnitude. Between an empty fracture and an obstacle fraction of $f = 0.3$ the transmissivity drops 2 orders of magnitude, then again almost 2 orders of magnitude between $f = 0.3$ and $f = 0.7$ and almost an order of magnitude between $f = 0.7$ and $f = 0.8$. Decreasing the fracture aperture 5 times, while keeping the obstacle diameter fixed, results in a more than 2 orders of magnitude transmissivity drop, if the obstacle fraction is small. On the other hand, the drop is less than an order of magnitude for a large obstacle fraction. For $\alpha = 1.0$, order of magnitude transmissivity drops are observed in the fraction intervals $f = 0–0.4$, $f = 0.4–0.65$, and $f = 0.65–0.8$. For $\alpha = 0.5$, the entire drop over the studied fraction range is less than 3 orders of magnitude, with only an order of magnitude reduction reached for $f = 0.5$. For a fixed obstacle diameter and at an intermediate fraction of $f = 0.3$, the impact of decreasing α from 1.0 to 0.5 corresponds to increasing obstacle fraction to about $f = 0.5$. For $\alpha = 0.1$, only an order of magnitude transmissivity drop is observed after covering 70% of the fracture area with obstacles. In general, the range of the observed transmissivities for different α values clearly decreases with increasing obstacle fraction. Figure 11 compares the numerically determined fracture permeabilities

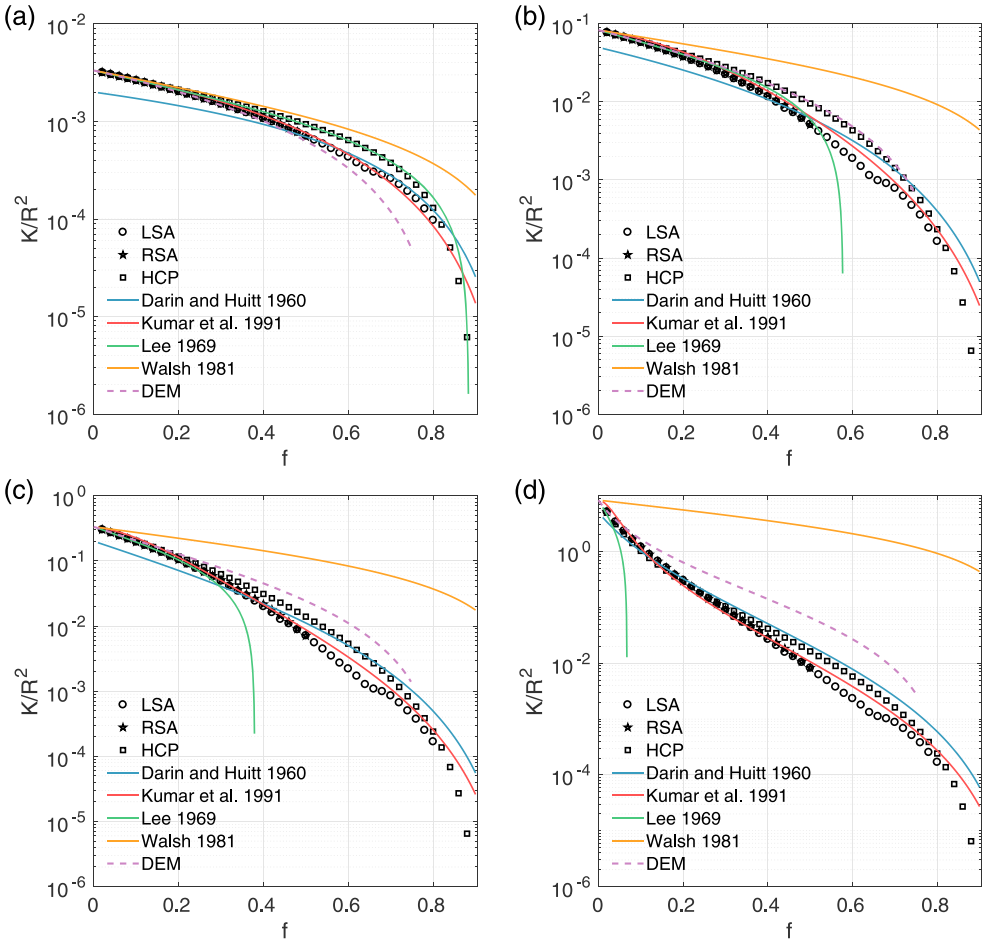

Figure 11. Effective medium scheme predictions for the normalized effective permeability of a plane-walled fracture with circular obstacles as a function of obstacle fraction for (a) $\alpha = 0.1$, (b) 0.5, (c) 1.0, and (d) 5.0. Solid lines show the predictions according to the models of Darin and Huitt (1960), Lee (1969), Walsh (1981), and Kumar et al. (1991), and the dashed lines give the effective permeability calculated using the differential effective medium (DEM) model developed based on the drag force formula from Spielman and Goren (1968). The results of numerical simulations are shown with the circular (LSA), triangular (RSA), and star (HCP) markers.

with the predictions of several selected effective medium schemes. Darin and Huitt (1960) proposed a modified Carman-Kozeny scheme for a plane-walled fracture containing partly embedded spherical grains

$$\frac{K}{R^2} = \frac{(1-f)^3}{CS^2f^2} \tag{24}$$

where Carman-Kozeny constant $C = C_v\tau^2$ contains information about obstacle shape factor C_v and hydraulic tortuosity τ (we use $C = 5$ following the original work of Darin and Huitt, 1960, which is a typical value for unconsolidated porous media), and S is the wetted surface area per unit volume of obstacles contained between the fracture faces. We have adjusted the original expression for S and f to the case of cylindrical obstacles rather than partly embedded spheres.

Spielman and Goren (1968) used the drag force (equation (22)) and the self-consistent averaging (SCA) technique to obtain an implicit relation between the effective conductivity and the obstacle fraction f for a fibrous material. The original SCA prediction is limited to fractions of up to 0.5, and it is not taking into account the underlying permeability of an empty fracture. Rather than modifying the SCA scheme, we develop a differential effective medium type of scheme (Norris, 1985) using equation (22)

$$\frac{ds}{df} = \frac{1}{1-\frac{f}{f_m}}\left(s + 2\frac{K_1(s)}{K_0(s)}\right) \tag{25}$$

where f_m is the random close packing fraction for monodisperse disks and K_0, K_1, and s are defined in section 3. We set $f_m = 0.82$ (Berryman, 1983) and numerically solve equation (25) using an ODE solver in MATLAB.

Lee (1969) constructed an approximate three-dimensional solution for circular cylinders periodically distributed on a hexagonal lattice between two parallel plates. For a large separation between the cylinders the following expression for the effective transmissivity was proposed

$$\frac{K}{R^2} = \frac{\alpha^2}{3}\frac{1 - f \cdot K_2\left(\frac{\pi}{2\alpha}\right)/K_0\left(\frac{\pi}{2\alpha}\right)}{1 + f \cdot K_2\left(\frac{\pi}{2\alpha}\right)/K_0\left(\frac{\pi}{2\alpha}\right)} \tag{26}$$

Based on the Reynolds flow model, Walsh (1981) used the Maxwell's effective medium approach to derive an analytical expression for the effective permeability of a fracture with randomly distributed circular cylindrical obstacles

$$\frac{K}{R^2} = \frac{\alpha^2}{3}\left(\frac{1-f}{1+f}\right) \tag{27}$$

Kumar et al. (1991) obtained an approximation to the overall velocity distribution across the fracture aperture based on a two-dimensional flow averaging in the fracture plane. By integrating the velocity profile, the following closed-form expression for the effective permeability was proposed

$$K = K_{2D}\left(1 - \frac{\tan h(\zeta)}{\zeta}\right) \tag{28}$$

where K_{2D} is the effective permeability of a two-dimensional Stokes flow across an array of parallel cylinders and $\zeta = \frac{(1-f)\alpha}{\sqrt{K_{2D}/R^2}}$. Depending on the obstacle geometry, expressions derived for either periodic (Drummond & Tahir, 1984; Hasimoto, 1959; Sangani & Yao, 1988) or randomly distributed cylinders (Kuwabara, 1959; Sangani & Yao, 1988) can be used. For an overview of the available models, we refer the readers to the papers of Åström et al. (1992), Skartsis et al. (1992), and Yazdchi et al. (2011). Here we use the classical model of Carman (1997), in the following form

$$\frac{K_{CK}}{R^2} = 4\frac{(1-f)^3}{\Psi_{CK} f^2} \tag{29}$$

where we set $\Psi_{CK} = 180$. Figure 11 shows the normalized effective permeability according to the predictions produced by the effective media schemes (equations (24)–(28)). For $f = 0.1$, the models of Kumar et al. (1991) and Lee (1969) give very good approximations to the numerical results obtained for LSA and HCP, respectively. As expected, the model of Walsh (1981) overestimates the effective permeability for large obstacle fractions, but it still provides a useful approximation. For $f = 0.1$, the DEM model tends to underestimate the transmissivity with increasing f, but the prediciton remains within a factor 3–4 even for $f = 0.8$. The model of Darin and Huitt (1960) gives a very good approximation for high fractions ($f > 0.4$), but it slightly falls below the numerical results for low obstacle fractions. In particlular, it is incapable of reproducing the exact transmissivity of an empty fracture. For $f = 0.5$, the model of Kumar et al. (1991) again gives a very good approximation to the LSA results over the entire range of the studied obstacle fractions. While the DEM scheme exhibits an almost perfect fit to the HCP results for all the fractions, the model of Lee (1969) only works well up to a fraction of about $f = 0.5$. The model of Darin and Huitt (1960) gives a good approximation, within a factor of 2, over the entire range of fractions. For high obstacle fractions, the model of Walsh (1981) overestimates the effective transmissivity by almost 2 orders of magnitude. For $f = 1.0$, both the models of Kumar et al. (1991) and Darin and Huitt (1960) give satisfactory approximations. The DEM model systematically overestimates the transmissivity, but the prediction is still close to the numerical results. The model of Lee (1969) can be only used for fractions up to $f = 0.3$, and it actually fails to deliver any result for fractions exceeding about 0.4. For $f = 5.0$, both the model of Walsh (1981) and Lee (1969) are not applicable. The models of Kumar et al. (1991) and Darin and Huitte (1960) remain to provide highly accurate approximations, and the DEM model notably overestimates the effective transmissivity, but it still captures the effective transmissivity within an order of magnitude for all the fractions. For large ζ, the model of Kumar et al. (1991) recovers the two-dimensional limit, that is, $\lim_{\zeta\to\infty} K = K_{2D}$. For small ζ,

$$K/K_{2D} \simeq \zeta^2/3 \tag{30}$$

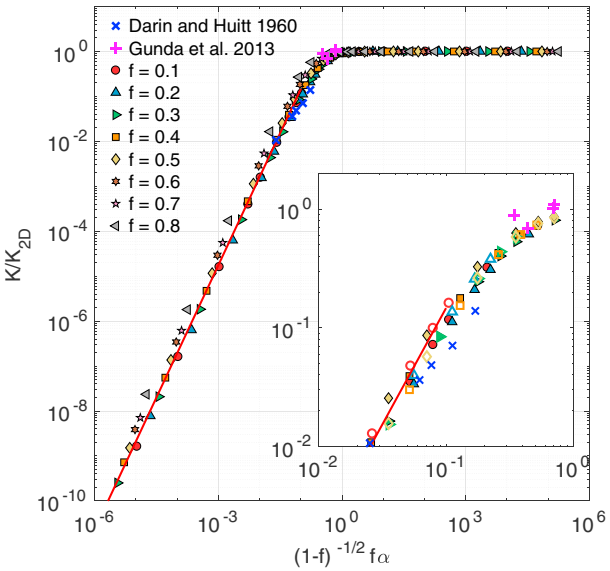

Figure 12. Normalized mean permeability K/K_{2D} as a function of $(1-f)^{-1/2}f\alpha$. The results are shown for LSA configurations and a wide range of obstacle fractions. Solid line gives the power law fit, which is consistent with the asymptotic scaling in the limit of small aperture and small fraction derived using the model of Kumar et al. (1991) and the Carman-Kozeny relationship. Experimental results: Darin and Huitt (1960) for random arrangement of spherical propping agent (blue cross) and of Gunda et al. (2013) for hexagonal array of cylindrical pillars in micofluid device (magenta plus sign). The experimental results are normalized by numerical value of K_{2D}. The figure inset presents close-up with numerical results in the fraction range $f = 0.1-0.5$; additional results for HCP configuration are marked by open symbols for comparison with experimental data of Gunda et al. (2013).

where Carman-Kozeny model gives

$$\zeta = \frac{\sqrt{\Psi_{CK}}}{2}(1-f)^{-\frac{1}{2}}f\alpha \tag{31}$$

Figure 12 shows the effective permeability data normalized by the numerically obtained K_{2D} (2-D Stokes simulations using infinite cylinders) as a function of $(1-f)^{-1/2}f\alpha$ parameter. A fair data collapse can be observed, although the data are shown for the entire range of obstacle fractions. The results show that the asymptotic effective conductivity computed for infinitely long cylinders (the 2-D Stokes model) is a good approximation once $(1-f)^{-1/2}f\alpha$ exceeds about $5 \cdot 10^{-1}$. Thus, α value at the transition yields about 1 for $f = 0.5$. In Figure 10, the transmissivity curves computed for $\alpha \geq 0.5$ are roughly parallel to each other for high enough fractions, and the effective permeability curves for $\alpha \geq 0.5$ should overlap if they were displayed in the same plot in Figure 11. For small values of $(1-f)^{-1/2}f\alpha$, the normalized effective permeability can be fairly well approximated by a power law fit (solid red line in Figure 12), particularly for low and medium packing fractions. The fit is obtained with a power law exponent of 2, and it gives a prefactor of 14.56, which is consistent with equations (30) and (31).

In Figure 12, we also present effective fracture permeabilities from two experimental works: Darin and Huitt (1960) and Gunda et al. (2013). Darin and Huitt (1960) performed measurements for random arrangements of spherical, partially embedded proppant grains (steal balls) placed in plane-walled fracture (steal plates) in a low packing fraction limit, that is, $f = 0.05-0.23$ and $\alpha = 0.35-0.82$. The discrepancy between numerical values for LSA configuration and experimental data are in the range of 12–38%; the smallest discrepancies are for low f and α, and the error increases with increasing f and α. This can be explained by the difference in the shape of the obstacles used in experiments (spheres) and numerical simulations (cylinders). Gunda et al. (2013) delivered experimental measurements of the effective permeability for hexagonally placed cylindrical pillars in a microfluidic device for low Reynolds number, that is, $Re < 1$, in packing fraction range $f = 0.1-0.5$ and $\alpha = 0.98-3.26$. The experimental data differ from our numerical results of HCP in the range of 1.7–33%.

6. Discussion

Fluid flow in rough-walled fracture is typically studied using the Reynolds model (Brown, 1987; Zimmerman et al., 1991). Mourzenko et al. (1995) discussed the validity of the Reynolds approximation as a function of fracture roughness characteristics. The Reynolds model is incapable of capturing recirculation flow developing within large embayments at the fracture walls and fulfiling the no-slip boundary condition at the rims of the contact area, which leads to an overestimated effective transmissivity. The Brinkman model (Brinkman, 1949) can be viewed as a hybrid model, combing the characteristics of the Darcy and Stokes models. Typical applications of the Brinkman model include porous flow in fibrous media (Spielman & Goren, 1968) and fluid flow in dual-porosity rocks such as karst reservoirs (Krotkiewski et al., 2011). In the case of fibrous media, the Brinkman model allows for applying the no-slip boundary condition at the interface between the impermeable obstacles and the porous matrix, and in dual-porosity media allows for a smooth matching of the solutions between the domains dominated by the open-space and porous flow.

In this work, we study single-phase flow in the void space of a plane-walled fracture filled with impermeable circular cylindrical obstacles. We treat the fracture as a two-dimensional porous medium, whose permeability is given by the cubic law, and compute the flow field using the upscaled Brinkman model. The model embeds the assumption of a strictly parabolic velocity distribution across the fracture depth, which is not exactly fulfiled in the vicinity of the obstacles and lateral walls (Flekkøy et al., 1995). Thus, the Brinkman model for fracture flow is only approximate. Although a higher-order model could be derived following the theoretical analysis presented in Thompson (1968) and Lee and Fung (1969), our numerical tests show that the mismatch between the effective transmissivities computed using the Brinkman model and the true 3-D Stokes model

stays below 10% for fractions as high as 0.5. Transmissivity changes of this order correspond to variations of either obstacle fraction or fracture aperture well below the implied uncertainty level for typical applications. On the other hand, the transmissivity obtained with the Reynolds models may be grossly overestimated (up to several tens of times for relevant geometrical parameters). Although the presented Brinkman model was discussed for single-phase fracture flows, it can be used for modeling multicomponent miscible fluid flows and, in general, advection-diffusion problems in plane-walled fractures with obstacles. However, our tests show that the mismatch between the local velocities in the Brinkman and the Stokes models can be much larger than the differences observed for the effective transmissivity. Also, the vertical component of the velocity is not vanishing in the three-dimensional model, and, thus, the differences in the dispersion characteristics between the upscaled and true models should be carefully studied.

Propped fractures provide the conductive pathways during production phase in unconventional (tight sands, coal beds, and shale formations) gas reservoirs (Economides & Nolte, 2000). In addition, they form the essential link for mediating fluids in the emerging concepts of CO_2 sequestration in shale formations (Kang et al., 2011; Liu & Wilcox, 2010; Middleton et al., 2015; Sun et al., 2013). Hydraulic stimulation is also used in geothermal applications (Legarth et al., 2005); however, significant fracture wall roughness in crystalline rocks and coarse-grained sediments promotes self-propping of hydraulic fractures, rendering proppant injections less necessary.

In our work, we have focused on the idealized case of a plane-walled fracture with a partial monolayer of monodisperse proppant grains, which are approximated as cylindrical circular obstacles, and some consideration should be given as to the model applicability to the real geometry of propped fractures. In general, the processes of proppant transport and settlement are complex and dependent on a large number of parameters including proppant density, fracking fluid properties, pumping rate, and fracture geometry. Unfortunately, the final distributions of proppant grains are virtually impossible to image nowadays, and direct numerical simulations of suspension flows in narrow apertures have just begun to emerge (Shiozawa & McClure, 2016; Tomac & Gutierrez, 2015). The monolayer configuration has been traditionally considered as either difficult or impossible to achieve and treated more of a curiosity rather than technologically relevant scenario (Harrington & Hannah, 1975; Wendorff & Alderman, 1969), however, this view has been challenged in recent works (Brannon et al., 2004; Palisch et al., 2010). It may in fact be that a general shift toward slickwater fracturing, and technological advances such as ultralight proppants (Gaurav et al., 2010) promote the developed of the monolayer configuration. Nevertheless, in our view, irrespective of the actual design and targets of any given hydraulic fracture treatment, the proppant distribution is likely to be heterogeneous and significant portions of stimulated fractures may be propped with either complete or partial monolayers or not propped at all. In particular, sparsely distributed proppant configurations are likely to develop in narrow secondary fractures, which are commonly present in stimulated shales.

Already Darin and Huitt (1960) demonstrated that a partial monolayer of large proppant grains may provide a higher fracture transmissivity than multilayer packings of smaller proppants giving a greater fracture width. However, the stimulated fracture with a single proppant layer are prone to the processes of proppant embedment and crushing, which readily operate under high effective confining stresses. Proppant crushing can be limited by either using highly spherical sand grains or tailored high-strength proppants such as sintered bauxite (Liang et al., 2016). Deformable proppants, which increase the load-bearing contact area while adjusting their shape to fracture walls, have been proposed to reduce both proppant crushing and embedment (Brannon et al., 2010). We note that the embedded and deformed proppants may be approximately treated as cylindrical obstacles. The shape of the proppant grains can be even further modified by pressure solution and chemical precipitation (Liang et al., 2016). Some early experiments on proppant embedment include the laboratory experiments of Volk et al. (1981), which showed that a fracture in a shale sample propped by a partial monolayer exceeding 50% areal coverage could resist aperture closure equally well as a sandstone sample. On the other hand, the shale sample exhibited a much more rapid fracture closure once the proppant fraction was reduced below 50%. In addition, hydraulic fracturing exposes shale formations to fluids of altered composition, which may lead to an accelerated creep and clay swelling, resulting in an high rate of proppant embedment and fracture aperture reduction (Alramahi & Sundberg, 2012). In general, the laboratory experiments show that decreasing proppant fraction in the partial monolayer can in principle increase the transmissivity (Brannon et al., 2004; Palisch et al., 2010); however, an opposite trend is also present due to an increased proppant embedment as the load-bearing area decreases (Alramahi & Sundberg, 2012). Khanna et al. (2012) used the Hertz contact theory to find the embedment of rigid spherical proppants into elastic fracture walls

as a function of proppant concentration and confining pressure. The transmissivity of the deformed fracture was calculated using computational fluid dynamics, and the optimal proppant fraction was found as a function of the load. The effective transmissivity is much more sensitive to the details of the proppant packings rather than the effects of proppant embedment for multilayer proppant configurations (Jansen et al., 2015; Zhang et al., 2015).

Round proppants with narrow size distribution are commonly used in fracture treatment, in a hope to provide highest fracture conductivity (Gallagher, 2011). Hence, our assumption of monodisperse circular obstacles seems to be plausible. On the other hand, disregarding fracure wall roughness may be a more restrictive assumption, as the lower range of the proppant grain size, which typically falls between 0.1 to 2 mm, coincides with the amplitude of the fracture wall roughness measured in shales (Pluymakers et al., 2017). It seems likely that for the partial monolayer configuration part of the load is transmitted through the contacts developed directly between the fracture walls. It is expected that fracture roughness may lead to a reduced transmissivity. It can be also speculated that processes such as fines migration, local turbulence, multiphase flow and capillary trapping, gel clogging, and geochemical precipitation may have a detrimental influence on the fracture transmissivity during the production phase.

Our numerical simulations show that fracture aperture and proppant size and fraction are the key parameters determining the effective transmissivity, and the ordering of the obstacles has a second-order effect. The effective medium model of Kumar et al. (1991) gives a very good approximation to the effective permeability (and transmissivity) of a plane-walled fracture with circular obstacles. Also, the prediction produced by the simple model of Darin and Huitt (1960) can be used for moderate and high obstacle fractions. We speculate that the performance of the differential effective medium scheme could be improved by introducing the effective viscosity into the model (Koplik et al., 1983; Lundgren, 1972; Martys et al., 1994). The effective medium schemes, which have been calibrated by numerical simulations, could be used to facilitate overall analysis of the effective transmissivity of propped fracture under in situ loads (e.g., Khanna et al., 2012). On the other hand, using the Reynolds model and the related effective medium schemes can lead to a gross overestimation of the fracture transmissivity and should be avoided for propped fractures.

Although the presented model is derived for a plane-walled fracture, it could still be used to provide first-order estimates to the effective transmissivity of rough-walled fractures by introducing an equivalent aperture and treating the contact areas as obstacles. The model can be directly used for manufactured systems such as microfluidic devices for microbiological filration or separation systems (Cady et al., 2003; Nagrath et al., 2007), high performance liquid chromatography (Song et al., 2012), dielectrophoretic platforms (Khoshmanesh et al., 2011), heat spreading, and dissipation system for microelectronic Ranjan et al. (2012), which are often characterized by aperture-to-diameter ratios exceeding 1.

7. Conclusions

We have studied the effective transmissivity of a plane-walled fracture with circular cylindrical obstacles, varying the obstacle fraction f and the ratio between the fracture aperture and the obstacle diameter α. We have used the 3-D Stokes, an approximate 2.5-D Brinkman, and 2.5-D Reynolds fracture flow models to compute the flow field. In conclusion,

1. Our unstructured FEM implementation of the Brinkman model is capable of reproducing the analytically calculated flow field around an isolated circular obstacle with a high accuracy. The numerical code can efficiently handle models with a large number of obstacles (up to 10,000), thus allowing for a systematic study using computational domains of a good representative size. On the other hand, direct numerical simulations based on the 3-D Stokes model are limited to a smaller number of obstacles and require substantially larger computational resources.
2. The effective transmissivity of a plane-walled fracture with multiple circular cylindrical obstacles compares favorably to the numerical results obtained with the 3-D Stokes model. For obstacle fractions up to 0.5 and $\alpha = 0.5 - 1.0$, the relative difference between the computed transmissivities is below 10%. On the other hand, the transmissivities obtained with the Reynolds model can be even 20 times too high.
3. For a given obstacle fraction, the average and standard deviation of the effective transmissivities computed for various realizations converge and decay to 0, respectively. Although the generating algorithms are expected to produce statistically isotropic obstacle distributions, the system size effect results in a weak structural anisotropy, which manifests in the anisotropy of the effective transmissivity. Both the standard

deviation of the effective mean transmissivity and the effective anisotropy factor scale with the inverse of the system size. The anisotropy factor is less than 0.1 for $L/R = 100$, and using 2,500 obstacles ensures that the standard deviation of the effective transmissivity is less than 5%.

4. We use the obstacle radius to normalize the effective transmissivity of a plane-walled fracture with circular cylindrical obstacles. For a propped fracture, the obstacle size can be directly related to the proppant size. Our systematic numerical simulations using the Brinkman model show that the normalized effective transmissivity is predominantly dependent on the obstacle fraction f and the fracture aperture to obstacle diameter ratio α. Although the anticlustered configurations (HCP) produced systematically higher transmissivities than the random configurations generated with either RSA or LSA, the effect of obstacle ordering on the transmissivity remains within a factor of 2. The effective transmissivity systematically decreases with increasing obstacle fraction and decreasing fracture aperture (decreasing α for a fixed obstacle radius). The results show, for example, that in terms of the effective transmissivity, decreasing α from 1.0 to 0.5 corresponds to increasing obstacle fraction from 0.3. to 0.5.
5. The effective medium model of Kumar et al. (1991) gives a highly accurate approximation to our numerical results over the entire studied range of f and α parameters. For $(1-f)^{-1/2}f\alpha > 0.5$, the effective permeability of a plane-walled fracture with circular cylindrical obstacles can be approximated with the permeability of the corresponding two-dimensional system with infinitely long cylinders. For low α values, the effective permeability can be approximated by $K/K_{2D} \simeq 15(1-f)^{-1}f^2\alpha^2$.
6. The presented numerical results and effective medium scheme validations can be used by petroleum engineers for estimating transmissivities of propped fractures under in situ conditions. The model can also be applied to microfluidic systems and for deriving first-order estimates of the effective transmissivity of rough-walled, natural fractures with load-bearing contact areas.

Acknowledgments
The authors thank M. Dzikowski for creative discussions on this work. The research has been performed in the framework of the ShaleSeq project (Physicochemical effects of CO_2 sequestration in the Pomeranian gas bearing shales) funded from Norway grants in the Polish-Norwegian Research Programme operated by the National Centre for Research and Development, grant POL-NOR/234198/100/2014. Numerical computations were performed using the Computational Geology Laboratory (PGI-NRI) group computer resources. The data supporting this paper are available online at Zenodo repository (https://zenodo.org/record/1009310#.WeHL19XLvF4) or by contacting the corresponding author at lukasz.jasinski@pgi.gov.pl.

References

Adler, P. M., & Thovert, J.-F. (1999). *Fractures and fracture networks*. Dordrecht, Netherlands: Kluwer Academic.
Alramahi, B., & Sundberg, M. (2012). Proppant embedment and conductivity of hydraulic fractures in shales. In *46th US Rock Mechanics/Geomechanics Symposium*. Chicago, IL: American Rock Mechanics Association.
Andersen, C., Rupke, L., Hasenclever, J., Grevemeyer, I., & Petersen, S. (2015). Fault geometry and permeability contrast control vent temperatures at the Logatchev 1 hydrothermal field, Mid-Atlantic Ridge. *Geology*, *43*, 51–54. https://doi.org/10.1130/G36113.1
Åström, B. T., Pipes, R. B., & Advani, S. G. (1992). On flow through aligned fiber beds and its application to composites processing. *Journal of Composite Materials*, *26*(9), 1351–1373. https://doi.org/10.1177/002199839202600907
Aydin, A. (2000). Fractures, faults, and hydrocarbon entrapment, migration and flow. *Marine and Petroleum Geology*, *17*(7), 797–814. https://doi.org/10.1016/S0264-8172(00)00020-9
Balsa, T. F. (1998). Secondary flow in a Hele-Shaw cell. *Journal of Fluid Mechanics*, *372*, 25–44. https://doi.org/10.1017/S0022112098002171
Berkowitz, B. (2002). Characterizing flow and transport in fractured geological media: A review. *Advances in Water Resources*, *25*(8), 861–884. https://doi.org/10.1016/S0309-1708(02)00042-8
Berkowitz, B., & Adler, P. M. (1998). Stereological analysis of fracture network structure in geological formations. *Journal of Geophysical Research*, *103*(B7), 15,339–15,360. https://doi.org/10.1029/98JB01072
Berryman, J. G. (1983). Random close packing of hard spheres and disks. *Physical Review A*, *27*(2), 1053. https://doi.org/10.1103/PhysRevA.27.1053
Bickle, M., & McKenzie, D. (1987). The transport of heat and matter by fluids during metamorphism. *Contributions to Mineralogy and Petrology*, *95*(3), 384–392. https://doi.org/10.1007/BF00371852
Brace, W. (1980). Permeability of crystalline and argillaceous rocks. *International Journal of Rock Mechanics and Mining Sciences & Geomechanics Abstracts*, *17*, 241–251. https://doi.org/10.1016/0148-9062(80) 90807-4
Brannon, H. D., Malone, M. R., Rickards, A. R., Wood, W. D., Edgeman, J. R., & Bryant, J. L. (2004). Maximizing fracture conductivity with proppant partial monolayers: Theoretical curiosity or highly productive reality? In *SPE Annual Technical Conference and Exhibition*. Houston, TX: Society of Petroleum Engineers. https://doi.org/10.2118/90698-MS
Brannon, H. D., Rickards, A. R., Stephenson, C. J., & Maharidge, R. L. (2010). Method of stimulating oil and gas wells using deformable proppants. uS Patent 7,789,147.
Brinkman, H. C. (1949). A calculation of the viscous force exerted by a flowing fluid on a dense swarm of particles. *Flow Turbulence and Combustion*, *1*(1), 27. https://doi.org/10.1007/BF02120313
Brown, S. R. (1987). Fluid flow through rock joints: The effect of surface roughness. *Journal of Geophysical Research*, *92*(B2), 1337–1347. https://doi.org/10.1029/JB092iB02p01337
Brush, D. J., & Thomson, N. R. (2003). Fluid flow in synthetic rough-walled fractures: Navier-Stokes, Stokes, and local cubic law simulations. *Water Resources Research*, *39*(4), 1085. https://doi.org/10.1029/2002WR001346
Budek, A., Kwiatkowski, K., & Szymczak, P. (2017). Effect of mobility ratio on interaction between the fingers in unstable growth processes. *Physical Review E*, *96*, 42218. https://doi.org/10.1103/PhysRevE.96.042218
Cady, N. C., Stelick, S., & Batt, C. A. (2003). Nucleic acid purification using microfabricated silicon structures. *Biosensors and Bioelectronics*, *19*(1), 59–66. https://doi.org/10.1016/S0956-5663(03)00123-4
Carman, P. (1997). Fluid flow through granular beds. *Chemical Engineering Research and Design*, *75*, S32–S48. https://doi.org/10.1016/S0263-8762(97)80003-2
Chernyakov, A. L. (2001). The viscous drag of a rough cylinder in a liquid flow in a porous medium. *Colloid Journal*, *63*(4), 499–505. https://doi.org/10.1023/A:1016770308900
Cooke, C. Jr. (1973). Conductivity of fracture proppants in multiple layers. *Journal of Petroleum Technology*, *25*(9), 1–101. https://doi.org/10.2118/4117-PA

Curewitz, D., & Karson, J. A. (1997). Structural settings of hydrothermal outflow: Fracture permeability maintained by fault propagation and interaction. *Journal of Volcanology and Geothermal Research*, *79*(3–4), 149–168. https://doi.org/10.1016/S0377-0273(97)00027-9

Dabrowski, M., Krotkiewski, M., & Schmid, D. (2008). Milamin: Matlab-based finite element method solver for large problems. *Geochemistry, Geophysics, Geosystems*, *9*, Q04030. https://doi.org/10.1029/2007GC001719

Darin, S., & Huitt, J. (1960). Effect of a partial monolayer of propping agent on fracture flow capacity. *Transactions AIME*, *219*, 31–37.

Detwiler, R. L., Glass, R. J., & Bourcier, W. L. (2003). Experimental observations of fracture dissolution: The role of Peclet number on evolving aperture variability. *Geophysical Research Letters*, *30*(12), 1648. https://doi.org/10.1029/2003GL017396

Dippenaar, M. A., & Rooy, J. L. V. (2016). On the cubic law and variably saturated flow through discrete open rough-walled discontinuities. *International Journal of Rock Mechanics and Mining Sciences*, *89*(Supplement C), 200–211. https://doi.org/10.1016/j.ijrmms.2016.09.011

Drummond, J., & Tahir, M. (1984). Laminar viscous flow through regular arrays of parallel solid cylinders. *International Journal of Multiphase Flow*, *10*(5), 515–540. https://doi.org/10.1016/0301-9322(84)90079-X

Durham, W. B., & Bonner, B. P. (1994). Self-propping and fluid flow in slightly offset joints at high effective pressures. *Journal of Geophysical Research*, *99*(B5), 9391–9399. https://doi.org/10.1029/94JB00242

Economides, M. J., & Nolte, K. G. (2000). *Reservoir stimulation* (Vol. 18). New York: Wiley.

Feder, J. (1980). Random sequential adsorption. *Journal of Theoretical Biology*, *87*(2), 237–254. https://doi.org/10.1016/0022-5193(80)90358-6

Fernandez, J., Kurowski, P., Limat, L., & Petitjeans, P. (2001). Wavelength selection of fingering instability inside Hele-Shaw cells. *Physics of Fluids*, *13*(11), 3120–3125. https://doi.org/10.1063/1.1410120

Ferrari, A., Jimenez-Martinez, J., Borgne, T. L., Méheust, Y., & Lunati, I. (2015). Challenges in modeling unstable two-phase flow experiments in porous micromodels. *Water Resources Research*, *51*, 1381–1400. https://doi.org/10.1002/2014WR016384

Flekkøy, E. G., Oxaal, U., Feder, J., & Jøssang, T. (1995). Hydrodynamic dispersion at stagnation points: Simulations and experiments. *Physical Review E*, *52*, 4952–4962. https://doi.org/10.1103/PhysRevE.52.4952

Gallagher, D. G. (2011). The hierarchy of oily conductivity. *Journal of Petroleum Technology*, *63*(4), 18–19.

Gaurav, A., Dao, E. K., & Mohanty, K. K. (2010). Ultra-lightweight proppants for shale gas fracturing. In *Tight Gas Completions Conference*. San Antonio, TX: Society of Petroleum Engineers. https://doi.org/10.2118/138319-MS

Ge, S. (1997). A governing equation for fluid flow in rough fractures. *Water Resources Research*, *33*(1), 53–61. https://doi.org/10.1029/96WR02588

Gunda, N. S. K., Joseph, J., Tamayol, A., Akbari, M., & Mitra, S. K. (2013). Measurement of pressure drop and flow resistance in microchannels with integrated micropillars. *Microfluidics and Nanofluidics*, *14*(3), 711–721. https://doi.org/10.1007/s10404-012-1089-1

Harrington, L., & Hannah, R. R. (1975). Fracturing design using perfect support fluids for selected fracture proppant concentrations in vertical fractures. In *Fall Meeting of the Society of Petroleum Engineers of AIME* Dallas, TX: Society of Petroleum Engineers. https://doi.org/10.2118/5642-MS

Hasimoto, H. (1959). On the periodic fundamental solutions of the Stokes equations and their application to viscous flow past a cubic array of spheres. *Journal of Fluid Mechanics*, *5*(2), 317–328. https://doi.org/10.1017/S0022112059000222

Hele-Shaw, H. S. (1898). The flow of water. *Nature*, *58*(1489), 33–36. https://doi.org/10.1038/058520a0

Horgue, P., Augier, F., Duru, P., Prat, M., & Quintard, M. (2013). Experimental and numerical study of two-phase flows in arrays of cylinders. *Chemical Engineering Science*, *102*, 335–345. https://doi.org/10.1016/j.ces.2013.08.031

Jamtveit, B., & Yardley, B. W. D. (1997). *Fluid flow and transport in rocks: An overview* (pp. 1–14). Netherlands, Dordrecht: Springer. https://doi.org/10.1007/978-94-009-1533-6

Jansen, T. A., Zhu, D., & Hill, A. D. (2015). The effect of rock mechanical properties on fracture conductivity for shale formations. In *SPE Hydraulic Fracturing Technology Conference*. The Woodlands, TX. Society of Petroleum Engineers. https://doi.org/10.2118/173347-MS

Kang, S. M., Fathi, E., Ambrose, R. J., Akkutlu, I. Y., & Sigal, R. F. (2011). Carbon dioxide storage capacity of organic-rich shales. *Spe Journal*, *16*(4), 842–855. https://doi.org/10.2118/134583-PA

Khanna, A., Kotousov, A., Sobey, J., & Weller, P. (2012). Conductivity of narrow fractures filled with a proppant monolayer. *Journal of Petroleum Science and Engineering*, *100*, 9–13. https://doi.org/10.1016/j.petrol.2012.11.016

Khoshmanesh, K., Nahavandi, S., Baratchi, S., Mitchell, A., & Kalantar-zadeh, K. (2011). Dielectrophoretic platforms for bio-microfluidic systems. *Biosensors and Bioelectronics*, *26*(5), 1800–1814. https://doi.org/10.1016/j.bios.2010.09.022

King, G. E. (2010). Thirty years of gas shale fracturing: What have we learned? In *SPE Annual Technical Conference and Exhibition*. Florence, Italy: Society of Petroleum Engineers. https://doi.org/10.2118/133456-MS

Koplik, J., Levine, H., & Zee, A. (1983). Viscosity renormalization in the Brinkman equation. *The Physics of Fluids*, *26*(10), 2864–2870. https://doi.org/10.1063/1.864050

Koza, Z., Matyka, M., & Khalili, A. (2009). Finite-size anisotropy in statistically uniform porous media. *Physical Review E*, *79*, 66306. https://doi.org/10.1103/PhysRevE.79.066306

Krotkiewski, M., & Dabrowski, M. (2013). MUTILS — A set of efficient modeling tools for multi-core CPUs implemented in MEX. EGU General Assembly 2013, held 7-12 April, 2013 in Vienna, Austria, id. EGU2013-7877.

Krotkiewski, M., Ligaarden, I. S., Lie, K.-A., & Schmid, D. W. (2011). On the importance of the Stokes-Brinkman equations for computing effective permeability in karst reservoirs. *Communications in Computational Physics*, *10*(5), 1315–1332.

Kumar, S., Zimmerman, R. W., & Bodvarsson, G. S. (1991). Permeability of a fracture with cylindrical asperities. *Fluid Dynamics Research*, *7*(3), 131–137. https://doi.org/10.1016/0169-5983(91)90053-L

Kuwabara, S. (1959). The forces experienced by randomly distributed parallel circular cylinders or spheres in a viscous flow at small Reynolds numbers. *Journal of the Physical Society of Japan*, *14*(4), 527–532. https://doi.org/10.1143/JPSJ.14.527

Laleian, A., Valocchi, A. J., & Werth, C. J. (2015). An incompressible, depth-averaged lattice Boltzmann method for liquid flow in microfluidic devices with variable aperture. *Computation*, *3*(4), 600–615. https://doi.org/10.3390/computation3040600

Landau, L., & Lifshitz, E. (1959). *Fluid mechanics* (Vol. 6). London: Pergamon Press.

Lauga, E., Brenner, M., & Stone, H. (2007). *Microfluidics: The no-slip boundary condition* (pp. 1219–1240). Berlin: Springer.

Lee, J. (1969). Slow viscous flow in a lung alveoli model. *Journal of Biomechanics*, *2*(2), 187–198. https://doi.org/10.1016/0021-9290(69)90030-X

Lee, J., & Fung, Y. (1969). Stokes flow around a circular cylindrical post confined between two parallel plates. *Journal of Fluid Mechanics*, *37*(4), 657–670. https://doi.org/10.1017/S0022112069000796

Lee, S. H., Lee, K.-K., & Yeo, I. W. (2014). Assessment of the validity of Stokes and Reynolds equations for fluid flow through a rough-walled fracture with flow imaging. *Geophysical Research Letters*, *41*, 4578–4585. https://doi.org/10.1002/2014GL060481

Legarth, B., Huenges, E., & Zimmermann, G. (2005). Hydraulic fracturing in a sedimentary geothermal reservoir: Results and implications. *International Journal of Rock Mechanics and Mining Sciences*, *42*(7), 1028–1041. https://doi.org/10.1016/j.ijrmms.2005.05.014

Liang, F., Sayed, M., Al-Muntasheri, G. A., Chang, F. F., & Li, L. (2016). A comprehensive review on proppant technologies. *Petroleum*, *2*(1), 26–39. https://doi.org/10.1016/j.petlm.2015.11.001

Lindblom, U. (1989). The performance of water curtains surrounding rock caverns used for gas storage. *International Journal of Rock Mechanics and Mining Sciences & Geomechanics Abstracts*, *26*(1), 85–97. https://doi.org/10.1016/0148-9062(89)90529-9

Liu, Y., & Wilcox, J. (2010). CO_2 adsorption on carbon models of organic constituents of gas shale and coal. *Environmental Science & Technology*, *45*(2), 809–814. https://doi.org/10.1021/es102700c

Lundgren, T. S. (1972). Slow flow through stationary random beds and suspensions of spheres. *Journal of Fluid Mechanics*, *51*(2), 273–299. https://doi.org/10.1017/S002211207200120X

Lupi, M., Geiger, S., & Graham, C. M. (2010). Hydrothermal fluid flow within a tectonically active rift-ridge transform junction: Tjörnes fracture zone, Iceland. *Journal of Geophysical Research*, *115*, B05104. https://doi.org/10.1029/2009JB006640

Mallikamas, W., & Rajaram, H. (2010). An improved two-dimensional depth-integrated flow equation for rough-walled fractures. *Water Resources Research*, *46*, w08506. https://doi.org/10.1029/2009WR008779

Martys, N., Bentz, D. P., & Garboczi, E. J. (1994). Computer simulation study of the effective viscosity in Brinkman's equation. *Physics of Fluids*, *6*(4), 1434–1439. https://doi.org/10.1063/1.868258

Matyka, M., Koza, Z., Gołembiewski, J., Kostur, M., & Januszewski, M. (2013). Anisotropy of flow in stochastically generated porous media. *Physical Review E*, *88*, 23018. https://doi.org/10.1103/PhysRevE.88.023018

Méheust, Y., & Schmittbuhl, J. (2001). Geometrical heterogeneities and permeability anisotropy of rough fractures. *Journal of Geophysical Research*, *106*(B2), 2089–2102. https://doi.org/10.1029/2000JB900306

Middleton, R. S., Carey, J. W., Currier, R. P., Hyman, J. D., Kang, Q., Karra, S., … Viswanathan, H. S. (2015). Shale gas and non-aqueous fracturing fluids: Opportunities and challenges for supercritical CO_2. *Applied Energy*, *147*, 500–509. https://doi.org/10.1016/j.apenergy.2015.03.023

Mourzenko, V., Thovert, J.-F., & Adler, P. (1995). Permeability of a single fracture; validity of the Reynolds equation. *Journal de Physique II*, *5*(3), 465–482. https://doi.org/10.1051/jp2:1995133

Mourzenko, V., Thovert, J.-F., & Adler, P. (1996). Geometry of simulated fractures. *Physical Review E*, *53*(6), 5606. https://doi.org/10.1103/PhysRevE.53.5606

Nagel, M., & Gallaire, F. (2015). Boundary elements method for microfluidic two-phase flows in shallow channels. *Computers & Fluids*, *107*, 272–284. https://doi.org/10.1016/j.compfluid.2014.10.016

Nagrath, S., Sequist, L. V., Maheswaran, S., Bell, D. W., Irimia, D., Ulkus, L., … Toner, M. (2007). Isolation of rare circulating tumour cells in cancer patients by microchip technology. *Nature*, *450*(7173), 1235–1239. https://doi.org/10.1038/nature06385

Neretnieks, I. (1990). Solute transport in fractured rock-applications to radionuclide waste repositories (Tech. Rep.). Stockholm, Sweden: Swedish Nuclear Fuel and Waste Management Co.

Norris, A. (1985). A differential scheme for the effective moduli of composites. *Mechanics of Materials*, *4*(1), 1–16. https://doi.org/10.1016/0167-6636(85)90002-X

Odling, N. E. (1997). Scaling and connectivity of joint systems in sandstones from western Norway. *Journal of Structural Geology*, *19*(10), 1257–1271. https://doi.org/10.1016/S0191-8141(97)00041-2

Oron, A. P., & Berkowitz, B. (1998). Flow in rock fractures: The local cubic law assumption reexamined. *Water Resources Research*, *34*(11), 2811–2825. https://doi.org/10.1029/98WR02285

Palisch, T. T., Vincent, M., & Handren, P. J. (2010). Slickwater fracturing: Food for thought. *SPE Production & Operations*, *25*(3), 327–344. https://doi.org/10.2118/115766-PA

Pluymakers, A., Kobchenko, M., & Renard, F. (2017). How microfracture roughness can be used to distinguish between exhumed cracks and in-situ flow paths in shales. *Journal of Structural Geology*, *94*, 87–97. https://doi.org/10.1016/j.jsg.2016.11.005

Pop, I., & Cheng, P. (1992). Flow past a circular cylinder embedded in a porous medium based on the Brinkman model. *International Journal of Engineering Science*, *30*(2), 257–262. https://doi.org/10.1016/0020-7225(92) 90058-O

Pruess, K., Wang, J., & Tsang, Y. (1990). On thermohydrologic conditions near high-level nuclear wastes emplaced in partially saturated fractured tuff: 1. Simulation studies with explicit consideration of fracture effects. *Water Resources Research*, *26*(6), 1235–1248. https://doi.org/10.1029/WR026i006p01235

Pyrak-Nolte, L. J., Myer, L. R., Cook, N. G., & Witherspoon, P. A. (1987). Hydraulic and mechanical properties of natural fractures in low permeability rock. In *6th ISRM Congress, International Society for Rock Mechanics*. Montreal, Canada.

Ramurthy, M., Magill, D. P., Sanchez, P. W., & Parker, M. A. (2013). Case history: Production results from partial monolayer proppant fracture treatments in the pictured cliffs formation horizontal wells of San Juan basin. In *SPE Hydraulic Fracturing Technology Conference*. The Woodlands, TX: Society of Petroleum Engineers. https://doi.org/10.2118/163815-MS

Ranjan, R., Patel, A., Garimella, S. V., & Murthy, J. Y. (2012). Wicking and thermal characteristics of micropillared structures for use in passive heat spreaders. *International Journal of Heat and Mass Transfer*, *55*(4), 586–596. https://doi.org/10.1016/j.ijheatmasstransfer.2011.10.053

Renard, F., Voisin, C., Marsan, D., & Schmittbuhl, J. (2006). High resolution 3D laser scanner measurements of a strike-slip fault quantify its morphological anisotropy at all scales. *Geophysical Research Letters*, *33*, L04305. https://doi.org/10.1029/2005GL025038

Renshaw, C. E. (1995). On the relationship between mechanical and hydraulic apertures in rough-walled fractures. *Journal of Geophysical Research*, *100*(B12), 24,629–24,636. https://doi.org/10.1029/95JB02159

Reynolds, O. (1886). On the theory of lubrication and its application to Mr. Beauchamp Tower's experiments, including an experimental determination of the viscosity of olive oil. *Proceedings of the Royal Society of London*, *40*(242–245), 191–203.

Sangani, A. S., & Yao, C. (1988). Transport processes in random arrays of cylinders. II. Viscous flow. *Physics of Fluids*, *31*(9), 2435–2444. https://doi.org/10.1063/1.866596

Shewchuk, J. R. (1996). Triangle: Engineering a 2D quality mesh generator and Delaunay triangulator. In M. C. Lin & D. Manocha (Eds.), *Applied computational geometry towards geometric engineering, Lecture Notes in Computer Science* (Vol. 1148, pp. 203–222). Berlin: Springer. https://doi.org/10.1007/BFb0014497

Shiozawa, S., & McClure, M. (2016). Comparison of pseudo-3D and fully-3D simulations of proppant transport in hydraulic fractures, including gravitational settling, formation of proppant banks, tip-screen out, and fracture closure. In *SPE Hydraulic Fracturing Technology Conference*. The Woodlands, TX: Society of Petroleum Engineers. https://doi.org/10.2118/179132-MS

Si, H. (2015). Tetgen, a Delaunay-based quality tetrahedral mesh generator. *ACM Transactions on Mathematical Software (TOMS)*, *41*(2), 11.

Skartsis, L., Kardos, J., & Khomami, B. (1992). Resin flow through fiber beds during composite manufacturing processes. Part I: Review of Newtonian flow through fiber beds. *Polymer Engineering & Science*, *32*(4), 221–230. https://doi.org/10.1002/pen.760320402

Skoge, M., Donev, A., Stillinger, F. H., & Torquato, S. (2006). Packing hyperspheres in high-dimensional Euclidean spaces. *Physical Review E*, *74*(4), 41127. https://doi.org/10.1103/PhysRevE.74.041127

Song, Y., Noguchi, M., Takatsuki, K., Sekiguchi, T., Mizuno, J., Funatsu, T., … Tsunoda, M. (2012). Integration of pillar array columns into a gradient elution system for pressure-driven liquid chromatography. *Analytical Chemistry*, *84*(11), 4739–4745. https://doi.org/10.1021/ac3001836

Spielman, L., & Goren, S. L. (1968). Model for predicting pressure drop and filtration efficiency in fibrous media. *Environmental Science & Technology*, *2*(4), 279–287. https://doi.org/10.1021/es60016a003

Stokes, G. G. (1851). *On the effect of the internal friction of fluids on the motion of pendulums* (Vol. 9). Cambridge: Pitt Press.

Sun, H., Yao, J., Gao, S.-h., Fan, D.-y., Wang, C.-C., & Sun, Z.-X. (2013). Numerical study of CO_2 enhanced natural gas recovery and sequestration in shale gas reservoirs. *International Journal of Greenhouse Gas Control*, *19*, 406–419. https://doi.org/10.1016/j.ijggc.2013.09.011

Szymczak, P., & Ladd, A. J. C. (2009). Wormhole formation in dissolving fractures. *Journal of Geophysical Research*, *114*, B06203. https://doi.org/10.1029/2008JB006122

Thompson, B. (1968). Secondary flow in a Hele-Shaw cell. *Journal of Fluid Mechanics*, *31*(2), 379–395. https://doi.org/10.1017/S0022112068000212

Tomac, I., & Gutierrez, M. (2015). Micromechanics of proppant agglomeration during settling in hydraulic fractures. *Journal of Petroleum Exploration and Production Technology*, *5*(4), 417–434. https://doi.org/10.1007/s13202-014-0151-9

Tsay, R.-Y., & Weinbaum, S. (1991). Viscous flow in a channel with periodic cross-bridging fibres: Exact solutions and Brinkman approximation. *Journal of Fluid Mechanics*, *226*, 125–148. https://doi.org/10.1017/S0022112091002318

Volk, L. J., Raible, C. J., Carroll, H. B., & Spears, J. S. (1981). Embedment of high strength proppant into low-permeability reservoir rock. In *SPE/DOE Low Permeability Gas Reservoirs Symposium*. Denver, CO: Society of Petroleum Engineers. https://doi.org/10.2118/9867-MS

Walsh, J. (1981). Effect of pore pressure and confining pressure on fracture permeability. *International Journal of Rock Mechanics and Mining Sciences & Geomechanics Abstracts*, *18*, 429–435. Elsevier https://doi.org/10.1016/0148-9062(81)90006-1

Wang, C. Y. (2009). Darcy-Brinkman flow with solid inclusions. *Chemical Engineering Communications*, *197*(3), 261–274. https://doi.org/10.1080/00986440903088603

Wang, L., Cardenas, M. B., Slottke, D. T., Ketcham, R. A., & Sharp, J. M. (2015). Modification of the local cubic law of fracture flow for weak inertia, tortuosity, and roughness. *Water Resources Research*, *51*, 2064–2080. https://doi.org/10.1002/2014WR015815

Wang, Z., Schmitt, D. R., & Wang, R. (2015). Does wettability influence seismic wave propagation in liquid-saturated porous rocks?. *Geophysical Journal International*, *203*(3), 2182–2188. https://doi.org/10.1093/gji/ggv434

Warpinski, N. R., Mayerhofer, M. J., Vincent, M. C., Cipolla, C. L., & Lolon, E. (2009). Stimulating unconventional reservoirs: Maximizing network growth while optimizing fracture conductivity. *Journal of Canadian Petroleum Technology*, *48*(10), 39–51. https://doi.org/10.2118/114173-PA

Wendorff, C., & Alderman, E. (1969). Prop-packed fractures—A reality on which productivity increase can be predicted, SPE Rocky Mountain Regional Meeting. https://doi.org/10.2118/2452-MS

Yazdchi, K., Srivastava, S., & Luding, S. (2011). Microstructural effects on the permeability of periodic fibrous porous media. *International Journal of Multiphase Flow*, *37*(8), 956–966. https://doi.org/10.1016/j.ijmultiphaseflow.2011.05.003

Yeo, W. (2001). Effect of contact obstacles on fluid flow in rock fractures. *Geosciences Journal*, *5*(2), 139–143.

Yoshida, H., Maejima, T., Nakajima, S., Nakamura, Y., & Yoshida, S. (2013). Features of fractures forming flow paths in granitic rock at an LPG storage site in the orogenic field of Japan. *Engineering Geology*, *152*(1), 77–86. https://doi.org/10.1016/j.enggeo.2012.10.007

Zeng, Y., & Weinbaum, S. (1994). Stokes flow through periodic orifices in a channel. *Journal of Fluid Mechanics*, *263*, 207–226. https://doi.org/10.1017/S0022112094004088

Zhang, J., Ouyang, L., Zhu, D., & Hill, A. (2015). Experimental and numerical studies of reduced fracture conductivity due to proppant embedment in the shale reservoir. *Journal of Petroleum Science and Engineering*, *130*, 37–45. https://doi.org/10.1016/j.petrol.2015.04.004

Zimmerman, R., Kumar, S., & Bodvarsson, G. (1991). Lubrication theory analysis of the permeability of rough-walled fractures. *International Journal of Rock Mechanics and Mining Sciences & Geomechanics Abstracts*, *28*, 325–331. https://doi.org/10.1016/0148-9062(91)90597-F

Zimmerman, R. W., & Bodvarsson, G. S. (1996). Hydraulic conductivity of rock fractures. *Transport in Porous Media*, *23*(1), 1–30. https://doi.org/10.1007/BF00145263

Zimmermann, G., & Reinicke, A. (2010). Hydraulic stimulation of a deep sandstone reservoir to develop an enhanced geothermal system: Laboratory and field experiments. *Geothermics*, *39*(1), 70–77. https://doi.org/10.1016/j.geothermics.2009.12.003